CERIA PROMOTED NO_X STORAGE AND REDUCTION MATERIALS

A THESIS

SUBMITTED TO THE DEPARTMENT OF CHEMISTRY AND

THE GRADUATE SCHOOL OF ENGINEERING AND SCIENCE OF

BILKENT UNIVERSTIY

IN PARTIAL FULFILLMENT OF THE REQUIREMENTS

FOR THE DEGREE OF

MASTER OF SCIENCE

By

ZAFER SAY

AUGUST 2011

To My Family
And
Esra Nur

ABSTRACT

CERIA PROMOTED NO_X STORAGE AND REDUCTION MATERIALS

ZAFER SAY

M.S in Chemistry

Supervisor: Assistant Prof. Dr. Emrah ÖZENSOY

In the current work, the effect of CeO_2 promotion on the NO_x storage materials and NO_x storage-reduction (NSR) catalysts is studied. Synthesized materials were prepared using different baria and ceria loadings in order to investigate the influence of the surface composition on the NO_x storage process. Synthesized materials were also thermally treated in the temperature range within 300 - 1273 K to mimic the thermal aging effects on the material structure. Structural properties of the synthesized materials were investigated via spectroscopic and diffraction techniques such as Raman spectroscopy, X-ray diffraction (XRD), and BET (Brunauer, Emmett, ve Teller) surface area analysis. These ex-situ characterization studies revealed that materials containing Pt showed indications of sintering after thermal treatment at elevated temperatures where Pt sites grew in size and were partially covered by BaO domains. Pt addition to the BaO/Al_2O_3 system facilitated the formation of the undesired $BaAl_2O_4$ phase, particularly at high baria loadings. Decomposition of the $Ba(NO_3)_2$ species took place at lower temperatures for Pt containing materials. An indication for a strong-metal-support interaction (SMSI) between Pt and CeO_2 sites was observed in Raman spectroscopic data, resulting in the formation of a new mixed oxide phase on the surface. BET results indicated that the specific surface area (SSA) of the synthesized materials monotonically decreased with increasing temperature and increasing BaO and CeO_2 loadings.

The behavior of the synthesized materials in NO_x and SO_x adsorption experiments were also investigated via temperature programmed desorption (TPD) and in-situ Fourier transform infrared (FTIR) spectroscopy. Ceria promotion had no significant influence on the nature of the adsorbed nitrate species and the NO_x uptake ability of the alumina support material. On the other hand, addition of Pt to CeO_2/Al_2O_3 binary and $BaO/CeO_2/Al_2O_3$ ternary systems was observed to enhance the NO_x storage. For the ternary mixed oxide NO_x storage systems ($BaO/CeO_2/Al_2O_3$), increasing BaO or CeO_2 loadings results in a decrease in the specific surface area values, which in turn leads to decreasing NO_x uptake. SO_2 (g) + O_2 (g) interaction with a selected set of samples were also investigated via in-situ FTIR spectroscopy. These experiments reveal that ceria promotion and platinum addition assisted the formation of surface sulfate species. Furthermore, the presence of ceria also resulted in a decrease in the thermal stability of sulfates and enabled easier regeneration.

Keywords: NSR, NO_x storage materials, γ-Al_2O_3, Ce/Al, Pt/Ce/Al, Ba/Ce/Al, Ba/Pt/Ce/Al, SO_x poisoning, XRD, Raman, BET, FTIR spectroscopy, TPD and XPS.

ÖZET

SERYUM DİOKSİT İLE ZENGİNLEŞTİRİLMİŞ NO_x DEPOLAMA VE İNDİRGEME KATALİZÖRLERİ

ZAFER SAY

Kimya Bölümü Yüksek Lisans Tezi

Tez Yöneticisi: Yard. Doç. Dr. Emrah Özensoy

Ağustos 2011

Bu çalışma kapsamında, seryum dioksitin NO_x depolama ve indergeme malzemeleri/katalizörleri üzerindeki etkisi incelenmektedir. Bu bağlamda, farklı miktarlarda Pt, CeO_2 ve BaO ile zenginleştirilmiş γ-Al_2O_3 destek/alttaş malzemesi içeren malzemeler sentezlenmiştir. Sentezlenen bu malzemelerinin yapısal karakterizasyonu, BET (Brunauer, Emmett, ve Teller) yüzey alanı ölçümleri, X-ışını kırınımı (XRD), Raman spektroskopisi teknikleri yardımıyla yapılmıştır. Elde edilen yapısal çözümleme sonuçları ışığında, platin ve alumina destek malzemesinin yüksek sıcaklıklarda faz değişikliğine uğramadığı gözlemlenmiştir. Platin metalinin Ba/Al depolama malzemesine eklenmesiyle, NO_x depolama kapasitesine olumsuz etkisi olduğu bilinen $BaAl_2O_4$, fazının yüksek sıcaklıklarda oluştuğu saptanmıştır. NO_x alım kapasitesine olumsuz yönde etki eden $BaAl_2O_4$ fazı, artan barium oksit miktarıyla doğru orantılı olarak artarken, sistemin CeO_2 ile zenginleştirilmesi, bu fazların oluşumunu önemli ölçüde azaltmaktadır. Sentezlenen malzemelere Pt eklenmesinin yapısal özellikler üzerindeki diğer bir etkisi ise, Pt birimlerinin CeO_2

ile girdiği kuvvetli etkileşimlerdir. Bu etkileşimler sonucu yüzeyde, Pt-O-CeO_2 türlerinin oluşumu Raman spektroskopisi yardımıyla gösterilmiştir. BET tekniği ile yaptığımız yüzey alanı ölçümlerinde ise CeO_2 ve BaO birimlerinin kütlece artan miktarda kullanılması sonucunda yüzey alanını azalmaktadır.

Sentezlemiş olduğumuz malzemelerin NO_x ve SO_x türü gazlarla etkileşimleri sıcaklık programlı yüzeyden buharlaştırma (TPD) ve Fourier Dönüşümlü Kızıl Ötesi Spektroskopisi (FTIR) teknikleri ile incelenmiştir. CeO_2 eklenmesinin alumina destek malzemesinin NO_x depolama kapasitesi üzerinde etkisi oldukça sınırlıdır. Fakat, Pt içeren Ce/Al ve Ba/Ce/Al türü destek malzemelerinin NO_x alım kapasiteleri, platin içermeyenlere nazaran daha yüksektir. Pt eklenmesinin diğer bir etkisi ise nitratların yüzeyden salınım sıcaklıklarıdır. Pt içeren malzemelerdeki nitrat salınımları, Pt içermeyenlere nazaran daha düşük sıcaklıklarda gerçekleşmektedir. Üçlü karışık oksit yapılarında (Ba/Ce/Al), BaO ve CeO_2 birimlerinin miktarlarının arttırlmasıyla, malzemelerin yüzey alanları azalmakta ve buna paralel olarak, NO_x depolama miktarları azalmaktadır. FTIR yöntemi kullanılarak sentezlenen bazı malzemelerin SO_2 (g) + O_2 (g) gaz karışımın ile etkileşimleri de incelenmiştir. Edinilen spektroskopik veriler, alumina destek malzemesinin CeO_2 ile zenginleştirimesi sonucu yüzeyde oluşan sülfatların miktarındaki artışı göstermektedir. Yüzey sülfatlarındaki artış, Pt metalinin Ce/Al ikili oksit yapısına eklenmesiyle de devam etmektedir. CeO_2 eklentisine dair diğer önemli sonuç ise CeO_2 içeren malzemeler üzerindeki sülfatların ısıl olarak daha az kararlı olmasıdır.

Anahtar Kelimeler: NSR, NO_x depolama malzemeleri, γ-Al_2O_3, Ce/Al, Pt/Ce/Al, Ba/Ce/Al, Ba/Pt/Ce/Al, SO_x zehirlenmesi, XRD, Raman, BET, FTIR spektroskopisi, TPD ve XPS.

ACKNOWLEDGEMENT

I would like to express my gratitude to…

My supervisor, Assistant Prof. Dr. Emrah Özensoy for his guidance, encouragement, patience and supervision throughout my studies.

Evgeny Vovk for his contributions and scientific discussions.

My parents; Ayşe and Mehmeti my sister Ebru and my brother İbrahim for their continuous supports throughout during my education.

Special thanks to my uncle, Sami Say, for his memorable helps and supports.

Finally, I am sincerely thankful to Esra Nur for her love and everlasting supports in my life.

TABLE OF CONTENTS

LIST OF FIGURES

LIST OF TABLES

1 INTRODUCTION:

Air pollution is one of the most challenging problems of the industrialized world. Thus, the legislations regarding the emissions of pollutants such as unburned hydrocarbons, CO_2, NO_x and SO_x are becoming constantly stricter every year [1]. The NO_x emitted from the mobile sources have serious destructive effects on the atmosphere, global ecosystem and especially on the human health. About one half of the total NO_x emissions results from mobile sources [2].

Due to the rigorous environmental regulations, automotive industry is forced to search for new promising technologies to lower the exhaust emissions. Three-way catalysts (TWC) were used for the reduction of toxic gases in conventional gasoline engines which operate under air to fuel ratios (A/F) equal to 14.5 as shown in Figure 1. For a better fuel economy and a more efficient combustion, diesel and lean burn gasoline engines have been considered as attractive alternatives which operate at A/F = 24. However, under such oxidizing (i.e. lean) conditions, hydrocarbons, NO_x cannot be efficiently reduced via a TWC system.

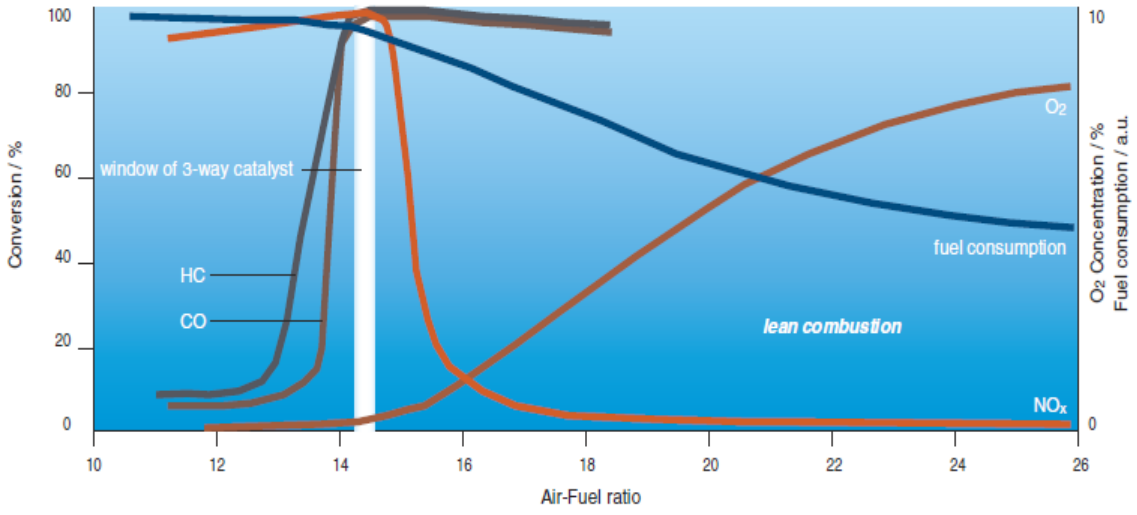

Figure 1: Fuel consumption and three-way performance of gasoline engines [3].

For lean burn engines, a promising after treatment method for the catalytic NO_x reduction from mobile sources is the NO_x storage/reduction (NSR) catalyst technology which was innovated by Toyota Motor Corporation [4,5]. NSR catalysts consist of three main components. These are the NO_x storage component based on alkaline and alkaline earth oxides (e.g. K, Ba, Sr), precious metal (e.g. Pt, Pd, Rh) which is responsible for the oxidation and reduction, and the high surface area support material (e.g. γ-Al_2O_3) [6].

NSR catalysts, which are also called Lean-NO_x Traps (LNT), operate under lean and rich conditions as shown in Figure 2. NO is the dominant NO_x species after combustion in the lean-burn engine. During the lean period (60-120 s), oxygen abundant period, NO is oxidized to NO_2 and this catalyst acts as lean NOx trap material storing NO_x as barium nitrates which is followed by short (5-15 s) rich period where most of the trapped NO_x is released and reduced to O_2 and N_2 by the help of unburned reducing hydrocarbons. After the completion of the rich period, resultant catalyst is regenerated and adsorption sites are mostly available for the next lean period. A commonly accepted view of the operation of the NSR catalysts is given below [3]:

$$NO \xrightarrow[Pt]{O_2} NO_2 \xrightarrow[Ba]{O_2} Ba(NO_3)_2$$

$$Ba(NO_3)_2 \xrightarrow{HC,\ H_2,\ CO} BaO + NO_2 \xrightarrow[Pt]{HC,\ H_2,\ CO} N_2 + CO_2 + H_2O$$

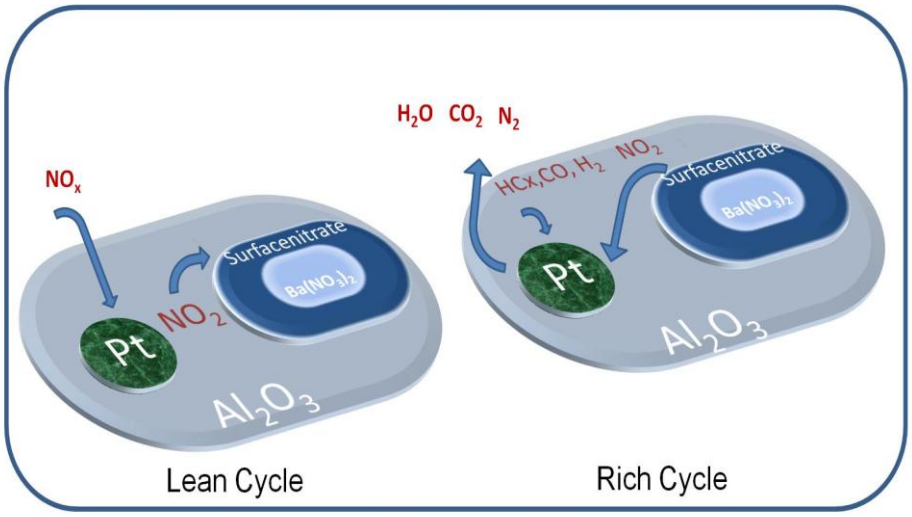

Figure 2: Illustration of the general operational principle of NSR catalyst

1.1 Material Properties of Oxides

Cerium oxide, CeO_2, has the fluorite (i.e. CaF_2) structure as shown in Figure 3. In the face centered cubic (FCC) structure of ceria, Ce^{4+} ions form a cubic close packed arrangement and all of the tetrahedral sites are occupied by the oxide ions whereas the octahedral sites remain vacant. In the literature, ceria is known to form oxygen deficient, non-stoichiometric CeO_{2-x}, at elevated temperatures [7,8]. Readily available lattice oxygen in the ceria structure has been exploited in catalytic reactions involving oxidation steps. The fluorite structure of ceria is retained up to 900 K under a reducing atmosphere. Above this temperature, ceria lattice starts to expand due to the reduction of Ce^{+4} to Ce^{+3} (due to the relatively larger ionic radius of Ce^{+3}). In the ceria structure, Ce and O atoms have coordination numbers of 8 and 4, respectively.

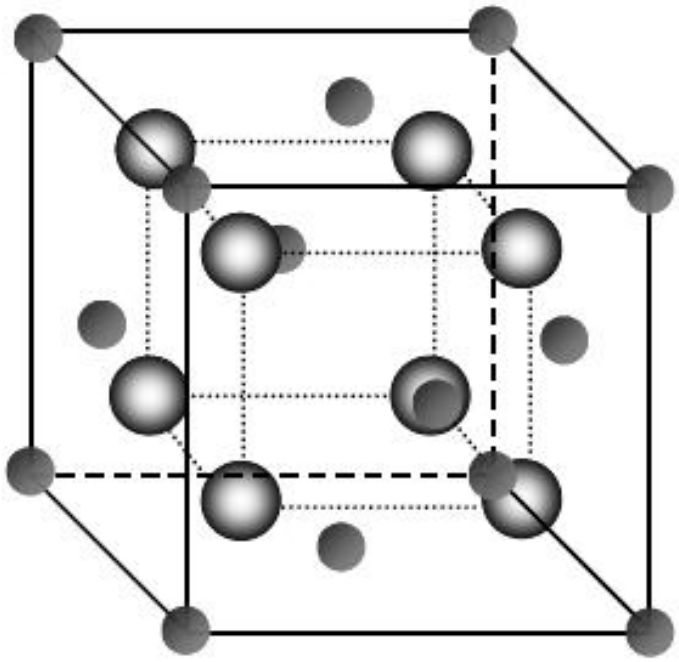

Figure 3: Fluorite structure of CeO_2 [9]

The main role of ceria and ceria based materials in TWC is to expand the operational A/F window and help maintaining the conversion efficiency of the catalyst. Ceria has the ability to store excess oxygen under the lean period and

release it under the rich conditions, which is used in the oxidation of CO and hydrocarbons in the downstream. This happens due to its ability to switch between Ce^{4+} and Ce^{3+} oxidation states depending on the oxygen partial pressure in the exhaust gas composition. Ceria can undergo a number of reactions by exchanging oxygen with gas molecules in the exhaust environment.

Under lean conditions:

$$Ce_2O_3 + 0.5\ O_2 \rightleftharpoons 2CeO_2$$

$$Ce_2O_3 + NO \rightleftharpoons 2CeO_2 + 0.5\ N_2$$

$$Ce_2O_3 + H_2O \rightleftharpoons 2CeO_2 + H_2$$

Under rich conditions:

$$2CeO_2 + H_2 \rightarrow Ce_2O_3 + H_2O$$

$$2CeO_2 + CO \rightarrow Ce_2O_3 + CO_2$$

γ-Al_2O_3 is the most commonly used oxide support in NSR formulations due to its porous structure with fine particle size, high surface area, high catalytic surface activity, distinctive chemical, mechanical and thermal properties [10-12]. γ-Al_2O_3 has a defective spinel structure (space group Fd3m), where the aluminum cations are located in the octahedral (O_h) and tetrahedral (T_d) interstitial sites identified by the face-centered-cubic (fcc) oxygen anion sublattice. At elevated temperatures γ-Al_2O_3 can go through polymorphic phase transitions to form other crystal structures which are commonly called as the transitional aluminas and eventually forms the thermodynamically stable α-Al_2O_3 (corundum) phase. This process is accompanied by a catastrophic loss of porosity via sintering. Another important part of the NSR system is the BaO component which crystallizes in a NaCl (rock salt) structure. The coordination number of both ions in the BaO lattice is 6.

1.2 Literature Survey in NSR

CeO_2 which is an important component of TWCs has been used as either a promoter [20] or a support material [21] in the NSR catalysts. Recent studies have shown that ceria can sacrifice itself to store some of the sulfur in the exhaust that leads to a greater number of barium sites available for NO_x storage [22-24]. The common use of ceria in the three way catalyst (TWC) is based on its oxygen storage capacity. Since the lattice oxygen atoms in ceria are quite mobile, it buffers the exhaust gas composition around the stoichiometric point (A/F =14.5) during the lean-rich cycle [25-28]. Ceria also enhances the precious metal dispersion [29,30] and is known as a promoter material for the water-gas shift (WGS) and steam reforming reactions [31-33] in the exhaust environment.

Although several studies employing FT-IR spectroscopy have been published in the literature, these studies mainly focused on $Pt/BaO/Al_2O_3$ type catalysts [34-45]. Ceria was found to improve NO_x storage capacity at low to moderate temperatures [21]. Philipp et al. [46] worked on NO and NO/O_2 co-adsorption on pure CeO_2 via DRIFT spectroscopy. While the NO adsorption leads to nitrite formation, due to co-adsorption of NO + O_2 mainly nitrates are formed. Later, Philipp et al. reported an extended study of NO_x adsorption on BaO/CeO_2 [47] and CeO_2 support was found to present a promising activity in reducing nitrates which is attributed to oxygen vacancies in the ceria lattice [48]. Cerium oxide has been also used as a promoter for the elimination of toxic exhaust gases in automobiles, composed mainly by platinum group metals supported on CeO_2/Al_2O_3[49,50].

Some of the possible routes of nitrite and nitrate formation on alumina surface due to NO_x adsorption are presented below[51]:

$3NO_2\ (g) + O^{2-}\ (surface) \rightarrow 2NO_3^-(ads) + NO\ (g)$

$2NO_2\ (g) + O^{2-}\ (surface) \rightarrow NO_3^-(ads) + NO_2^-\ (ads)$

Mechanism of reduction of stored nitrate species by the reductants such as CO and H_2 during rich period is the following [52,53]:

$Ba(NO_3)_2 + 5CO \rightarrow N_2 + BaO + 5CO_2$

$Ba(NO_3)_2 + 5H_2 \rightarrow N_2 + BaO + 5H_2O$

The decomposition of Ba nitrites and nitrates may occur according to following stoichiometry:

$Ba(NO_2)_2 \rightarrow 2NO + 1/2\ O_2 + BaO$

$Ba(NO_2)_2 \rightarrow 2NO + BaO_2$

$Ba(NO_3)_2 \rightarrow 2NO + 3/2\ O_2 + BaO$

$Ba(NO_3)_2 \rightarrow 2NO + O_2 + BaO_2$

FTIR investigations also demonstrated that NO_x storage in BaO/Al_2O_3 was enhanced in the presence of Pt. It was argued that Pt sites provided atomic oxygen to Ba and Al sites which catalyzed the formation of Ba- and Al- nitrates from nitrite species [54]:

$Ba(NO_2)_2 + 2\ O\text{-}Pt \rightarrow Ba(NO_3)_2$

NO adsorption experiments for $Pt\text{-}BaO/Al_2O_3$ showed that NO decomposed on Pt and NO was also oxidized to NO_2 via oxygen adatoms by the following possible reactions [55]:

$NO + Pt \rightarrow Pt\text{-}NO$

$Pt\text{-}NO + Pt \rightarrow Pt\text{-}N + Pt\text{-}O$

$Pt\text{-}NO + Pt\text{-}O \rightarrow NO_2 + 2Pt$

It was also proposed in the literature that during the NO exposure, Pt sites could lose their activity for NO decomposition due to the accumulation of atomic oxygen on the Pt sites. However, BaO sites that are in close proximity of the Pt particles was suggested to facilitate the spillover of the oxygen adatoms from Pt to BaO making Pt sites free of NO [55]. This spillover phenomenon may also lead to the formation of BaO_2 species as follows:

$O\text{-}Pt + BaO \rightarrow BaO_2 + Pt$

Some of the major drawbacks of NSR catalysts are the sulfur poisoning and thermal aging that may lead to the formation of $BaAl_2O_4$ and $BaCeO_3$, as well as the growth of Pt particles [56,57]. The formation of these undesired side processes leads to a decrease in NO_x storage capacity [58,59]. The origin of the sulfur species in the NSR system is the sulfur that is present in the fuel and engine lubricants. Even though sulfur contamination in the fuel is significantly reduced over the years, complete removal of sulfur has not been achieved. During the combustion of fuel, sulfur present in the fuel is converted into SO_2 and oxidized to SO_3 through the lean period via precious metals, such as Pt, Pd, Rh, etc. $BaSO_4$ formation is much slower than the $Ba(NO_3)_2$ formation [60]. However, the storage component (i.e. BaO) has a greater affinity towards SO_3 resulting in the formation of $BaSO_4$ which is thermodynamically more stable than $Ba(NO_3)_2$ [61]. Therefore, NSR catalysts are poisoned due to the loss of the available adsorption sites. Sulfur poisoning typically leads to the formation of alkaline earth metal and precious metal sulfate or sulfite complexes.

Studies on the deactivation of NO_x storage catalysts due to sulfur have also shown that (i) the deactivation rate increases with increased sulfur exposure [62]; (ii) compounds such as H_2S and COS deactivate the NO_x storage capacity in a way that is similar to the way in which SO_2 does [63,64]; (iii) between 250 and 450 °C the exposure to SO_2 decreases the catalytic activity for NO oxidation during the lean cycle and the NO_x reduction capacity of the precious metal during the rich cycle due to sulfur accumulation on the precious metal sites [65]; (iv) sulfur deactivation occurs much quicker under rich conditions than the lean conditions [66]; (v) exposure to SO_2 or $SO_2 + O_2$ results in the formation of $BaSO_4$ by a gradual removal of $BaCO_3$ [63,67]; (vi) small $BaSO_4$ particles are more easily decomposed than the large $BaSO_4$ particles [68]; and (vii) the decomposition of $BaSO_4$ requires a high-temperature regeneration treatment [69], but the presence of water decreases the decomposition temperature of $BaSO_4$.

The study of oxidative SO_2 adsorption on pure Al_2O_3 and pure CeO_2 support has been investigated by means of Infrared spectroscopy [70-72]. Waqif and co-

workers extended their focus on SO_2 adsorption by investigating solid mixture of CeO_2-Al_2O_3 by IR spectroscopy and compared that of pure alumina and ceria with previous studies [73-75]. Ji et al. [76] showed the effect of ceria addition on the sulfur resistance of NSR systems via DRIFT spectroscopy. Recently, a high surface area Pt/BaO/CeO_2 catalyst was prepared, showing higher sulfur tolerance than the Al_2O_3 based one [24].

In TWCs, noble metals such as Pt, Pd, Rh play an important role in the nature of sulfate species formed. Bazin et al [77] reported that sulfation on ceria is independent of the presence of Pt. However, previous works have shown that Pt favors the sulfate formation and reduction by H_2 on alumina [78-80]. Luo et al. [81] described the adsorption and reaction of SO_2 by using Pd rather than Pt. Similar results were reported by Yu and Shaw [82] who indicated increased sulfate formation on Pd/Al_2O_3 with respect to pure alumina. For ceria promoted alumina and pure ceria, addition of Pd lowers the amount of adsorbed sulfate species [83,84]. Mowery and McCormick [85] suggested that SO_2 adsorbed on PdO spillovers from the active palladium phase to the support leading to PdO sites to stay fresh longer with a relatively limited deactivation. Kylhammar et al. [86] studied adsorption of sulfur dioxide for CeO_2 and Pt/ CeO_2 samples at two different temperatures, 250 °C and 400 °C. It was shown that the rate of the formation of bulk sulfate for Pt/ CeO_2 is faster at 400 °C rather than 250 °C.

Abdulhamid et al. [87] published an extended article on SO_2 interaction with NSR catalyst and investigate different sulfate species on different samples such as, Al_2O_3, Pt/Al_2O_3, $BaCO_3$/Al_2O_3 and Pt/$BaCO_3$/Al_2O_3. The influence of the noble metal on sulfite formation was also investigated in this former study and sulfite formation was found to be enhanced with Pt addition. Su et al. [88] performed very similar SO_2 adsorption experiments on Al_2O_3, Pt/Al_2O_3 and Pt/BaO/Al_2O_3. Difference between two studies is the amount of SO_2 exposure. Su has used 1000 ppm SO_2 which was an order of magnitude larger than what Abdulhamid used. Especially for the Pt/Al_2O_3 catalyst, there is no evidence for sulfite species at higher SO_2 dosage while it is clearly observed in Abdulhamid's study [87].

Despite the numerous studies directed to investigations on the interactions of exhaust gases with different oxide surfaces so far, unfortunately many of the results are contradictory and specific spectroscopic details of the effect of CeO_2 on the storage behavior of the Al_2O_3, Ba/Al_2O_3 and $Pt/Ba/Al_2O_3$ system remain unclear in the open literature. Consequently, in the current study, the interactions of exhaust gases with different ceria promoted NOx storage materials and NSR catalysts have been investigated.

2 EXPERIMENTAL:

2.1 Sample Preparation

2.1.1Pt/Al catalyst

Alumina was impregnated with $Pt(NH_3)_2(NO_2)_2$ solution. The sample was dried at 353 K overnight, calcined in air at 873 K for 2 hours.

2.1.2 Ba/1Pt/Al catalyst

Alumina was impregnated with $Pt(NH_3)_2(NO_2)_2$ solution. Next, the sample was dried at 353 K overnight, calcined in air at 873 K for 2 hours. Then sample was impregnated with $Ba(NO_3)_2$.

2.1.3 Synthesis of CeO_2/Al_2O_3 Support Materials

Binary oxide CeO_2/Al_2O_3 materials were synthesized by incipient wetness impregnation of γ-Al_2O_3 (PURALOX, 200 m^2/g, SASOL GmbH, Germany). Support material was impregnated with aqueous solutions of $Ce(NO_3)_3.6H_2O$ (Fluka, Cerium(III) nitrate Hexahydrate, France) with different ceria (10 and 20 wt % CeO_2) loadings. During the impregnation of the ceria precursor, mixture was constantly stirred and then dried for 8 hours at 353 K. After the removal of water, Ce/Al support material was thermally treated under Ar(g) flow within 323 K-1273 K.

2.1.4 Synthesis of $Pt/CeO_2/Al_2O_3$

The binary oxide CeO_2/Al_2O_3 is impregnated with a solution of $Pt(NH_3)_2(NO_2)_2$ (Aldrich, Diamminedinitritoplatinum(II), 3.4 wt.% solution in dilute NH_3). Mixture was stirred and then dried for 8 hours at 353 K. After the removal of water, Ce/Al support material is thermally treated under Ar(g) flow within 323 K-1273 K.

2.1.5 Synthesis of $BaO/CeO_2/Al_2O_3$

Different set of NO_x storage materials in the form of $BaO/CeO_2/Al_2O_3$ ternary oxides with different BaO (8 and 20 wt % BaO) and Ce (10 and 20 wt % CeO_2) loadings were synthesized via incipient wetness impregnation. CeO_2/Al_2O_3 binary

oxide material was impregnated by aqueous solutions of barium nitrate (ACS Reagent, ≥ 99 %, Riedel-de Häen, Germany). Synthesized materials were also thermally treated within 323 K and 1273 K in Ar(g) flow. Structural properties of each of the synthesized materials was investigated with ex-situ characterization techniques including Raman spectroscopy, X-ray diffraction (XRD), and BET specific surface area analysis.

2.1.6 Synthesis of $BaO/Pt/CeO_2/Al_2O_3$

$Pt/CeO_2/Al_2O_3$ system was impregnated with a solution of $Pt(NH_3)_2(NO_2)_2$ (Aldrich, Diamminedinitritoplatinum(II), 3.4 wt.% solution in dilute NH_3). System was stirred and then dried for 8 hours at 353 K. Next, the synthesized materials were thermally treated within 323 K and 1273 K in Ar(g) flow.

2.1.7 Synthesis of BaO/CeO_2

CeO_2 (Inframad, nanopowder) support material was impregnated with a $Ba(NO_3)_2$ aqueous solution. Then, material was heated to 873 K for 2 hours under Ar(g) flow.

Synthesized materials with different loadings are listed in Table 1;

Sample	%Ceria	%Baria	%Pt	%Alumina
10Ce/Al	10	-	-	90
20Ce/Al	20	-	-	80
1Pt/10Ce/Al	10	-	1	90
1Pt/20Ce/Al	20		1	80
8Ba/1Pt/Al	-	8	1	92
20Ba/1Pt/Al	-	20	1	80
8Ba/10Ce/Al	10	8	-	92
8Ba/1Pt/10Ce/Al	10	8	1	92
20Ba/1Pt/10Ce/Al	10	20	1	80
8Ba/1Pt/20Ce/Al	20	8	1	92

Table 1: Sample compositions of the synthesized materials and the abbreviations used for each sample.

2.2 Experimental Techniques

2.2.1 FTIR:

IR spectroscopic measurements were carried in transmission mode in a batch-type spectroscopic reactor. FTIR spectrometer (Bruker Tensor 27) and catalytic reactor is combined with a quadruple mass spectrometer (QMS) (Stanford Research Systems, RGA 200) for temperature programmed reduction (TPD) and residual gas analyzer (RGA) experiments. FTIR data are recorded via Hg-Cd-Te (MCT) detector which operates with liquid nitrogen (LN_2) cooling. Each spectrum was obtained by averaging 128 scans with a $4cm^{-1}$ spectral resolution. Powder samples were pressed onto a high conductance and lithographically-etched tungsten grid (P/N PW10379-003). W-grid is attached to copper holder legs assembled to a ceramic vacuum feedthrough. In order to monitor the temperature, a K-type thermocouple which was spot-welded onto a tantalum foil was attached on the W-grid. Sample temperature was controlled between 300 K - 1173 K by an adjustable dc power supply and computer controlled PID electronics. About 20 mg of finely grounded sample was pressed onto the W-grid before the FTIR analysis. After having mounted the sample inside the batch reactor, it was outgassed at 373K for at least 12 hours in order to remove the water from sample surface while simultaneously baking the chamber walls. Prior to each adsorption experiment, samples were activated by flushing the reactor with 10 Torr of O_2 followed by evacuation and subsequent heating at 773 K (with a heating rate of 12 K min^{-1}. This procedure allowed us to obtain sample surfaces that were free of adsorbates/contaminants, sample was flashed to 773 K. Background IR spectrum of the clean and adsorbate free-sample was taken at 323K in vacuum before the acquisition of the sample spectra.

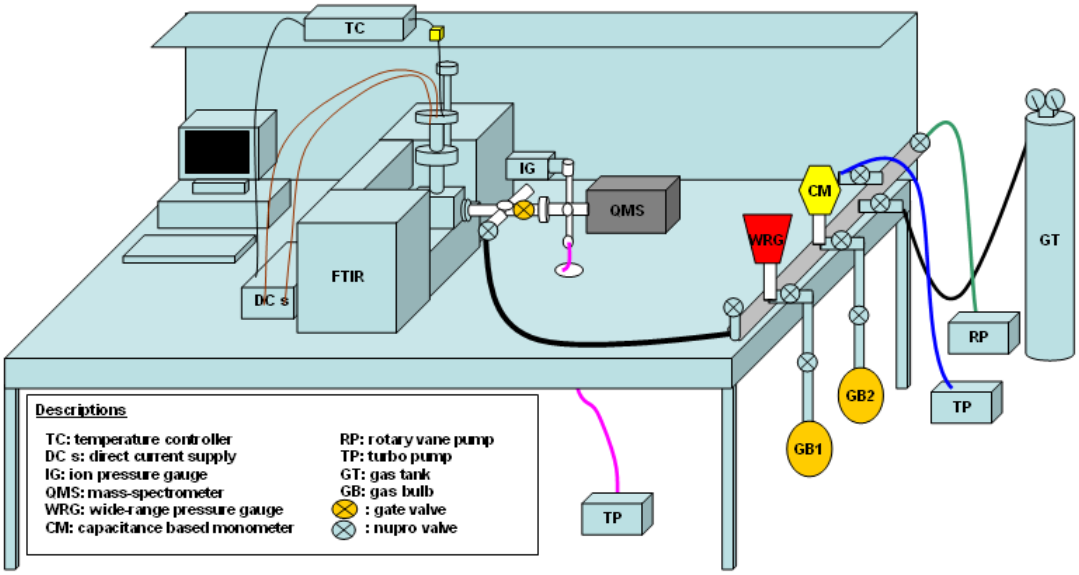

Figure 4: Simplified schematic of the custom-designed insitu-FTIR catalytic analysis system coupled to the quadrupole mass spectrometer chamber. Abbreviations used in the scheme are given in the inset. [89]

2.2.1.1 Stepwise NO_2 (g) adsorption experiments:

NO_2(g) was dosed onto an activated fresh sample. During the NO_2(g) exposure, gas pressure was controlled by a MKS Baratron absolute pressure transducer. In each dosing step, sample was exposed to 0.1 Torr of NO_2(g) for 1 min at 323 K. After the exposure and before taking the sample IR spectrum, gas phase inside the chamber was evacuated with rotary and turbo pumps until ~10^{-3} Torr is reached inside the reactor, before the next NO_2(g) dose. After multiple doses, a final saturation exposure was performed at 323 K where the sample was exposed to 8.0 Torr NO_2(g) for 10 min. All spectra were obtained at 323 K.

2.2.1.2 Temperature dependent FTIR experiments:

After the saturation of the freshly prepared samples with NO_2(g) (using a 8.0 Torr NO_2(g) exposure for 10 min at 323 K), thermal stability of the adsorbed species has been investigated. For the removal of the adsorbed species from the sample surfaces, temperature was linearly ramped to a certain value within 323 - 773 K. Then, the sample was cooled to 323 K and the FTIR spectrum was acquired in vacuum. This procedure was repeated with 50 K increments between 323 K - 773 K for the thermal stability analysis via FTIR.

2.2.1.3 SO_2 (g) + O_2 (g) adsorption experiments:

SO_2 (g)+O_2 (g) mixture was prepared with a SO_2/O_2 pressure ratio of 1/10. Before the adsorption experiments, material surface was activated by heating to 773 K in 10 Torr oxygen atmosphere followed by evacuation at 323 K. Then the background spectrum was obtained at 323 K in vacuum. First, the sample spectrum was acquired at 323 K after 10 min SO_2 (g)+O_2 (g) (P_{Total} =1.0 Torr) exposure. Next, the sample was heated at various temperatures ($T \leq 673$ K) in the presence of the gas mixture. After each heating step, sample was cooled to 323 K in the presence of the gas mixture for the FTIR data acquisition. Next, IR cell was evacuated at 323 K until a system pressure of 10^{-3} Torr was reached. This is followed by a similar data collection procedure where the sample was heated to various temperatures in vacuum and after each heating step, the sample was cooled to 323 K for IR data acquisition.

2.2.1.3 NO_x adsorption experiments on pre-poisoned samples:

In these set of experiments, the samples were activated by dosing 2.0 Torr of NO_2 over the sample for 10 min and then heated at 973 K to remove the NO_x on the material surface and eliminate other contaminants (such as carbonaceous species, water or pump oil inside the reactor). Poisoning of the materials were achieved by introducing 2.0 Torr SO_2 + O_2 (SO_2:O_2, 0.1:1) on the activated sample at 323 K and further heating in the gaseous mixture to 673 K for 20 min. Then, the system was evacuated at 323 K ($P_{reactor} < 1x10^{-3}$), prior to NO_2 adsorption. Next, the poisoned sample was exposed to 8 Torr of NO_2 at 323 K for 10 min in order to saturate the

poisoned sample surface with NO_x. Finally, the reactor was evacuated ($P_{reactor} < 1x10^{-3}$) at 323 K and FTIR spectrum of the sample was obtained.

2.2.2 BET

A Micromeritics Tristar 3000 surface area and porosity analyzer has been used for the BET specific surface area (SSA) measurements. SSA values were measured via low-temperature (LN_2 temperature) isothermal adsorption-desorption of N_2. Before the SSA measurements, 0.1g of the sample material was evacuated at 623 K for 3 hr in order to remove water, CO_2 and hydrocarbons from the pores inside the sample. After the outgassing is completed, the net mass loss of the sample was measured for the SSA calculations.

2.2.3 X-Ray Diffraction (XRD)

The XRD patterns were recorded using a Rigaku Miniflex diffractometer, equip

ed with a Miniflex goniometer and an X-ray source with Cu$K\alpha$ radiation, at λ = 1.54 Å, 30 kV and 15 mA. The powder samples were pressed and affixed onto standard-sized glass slides and scanned within the 10–80^o, 2θ range with a scan rate of 0.01^o s^{-1}. Diffraction patterns were assigned using Joint Committee on Powder Diffraction Standards (JCPDS) cards supplied by the International Centre for Diffraction Database (ICDD).

2.2.4 Raman Spectroscopy

The Raman spectra were recorded under ambient conditions using a HORIBA Jobin Yvon LabRam HR 800 instrument, equipped with a confocal Raman BX41 microscope, spectrograph with an 800 mm focal length and a CCD detector. The Raman spectrometer was equipped with a Nd: YAG laser (λ = 532.1 nm). While the Raman experiments were conducted, the laser power was tuned to 20 mW, measured at the sample position, in order to minimize the sample heating effects. All the powder samples were mechanically dispersed onto a single-crystal Si holder. The

incident light source was dispersed by a holographic grating with 600 grooves/mm and focused onto the sample using a 50X objective. The confocal hole and slit entrance were set at 1100 and 200 μm, respectively. The spectrometer was regularly calibrated by adjusting the zero-order position of the grating and comparing the measured Si Raman band frequency with the typical reference value of 520.7 cm^{-1}. All Raman spectra were acquired within 100-4000 cm^{-1} with an acquisition time of 213 s and a spectral resolution of 4 $cm^{-1.}$

2.2.5 Temperature Programmed Desorption (TPD)

2.2.5.1 Thermal Stability of NO_x species on Fresh Materials

TPD experiments were acquired by using a QMS, which was directly connected to the vacuum chamber through a pneumatic gate valve. The powder sample (mass = c.a. 20 mg) was pressed onto a tungsten grid which was mounted in the IR/TPD cell, as described above. Prior to each TPD data, oxidation-resistant thoria coated iridium filament of the mass spectrometer was outgassed for 30 min. After cooling to 323 K, the sample was exposed to 8 Torr of NO_2 for 20 min until the equilibrium was reached. Next, the system was outgassed at 1 x 10^{-6} Torr in order to remove the weakly physisorbed molecules. Subsequently, TPD experiments were carried out. Thermally evolving NO_x species during the desorption sequence were monitored by recording the QMS signals with mass to charge ratios (m/z) equal to 18 (H_2O), 28 (N_2/CO), 30 (NO), 32 (O_2), 44 (N_2O/CO_2) and 46 (NO_2) in pressure vs. time mode. A linear temperature ramp within the range of 323 – 1023 K was used during the TPD experiments where the ramp rate was 12 K/min. In order to ensure the reproducibility of the results, TPD experiments were performed multiple times for each sample.

3. RESULTS AND DISCUSSION

3.1 Structural Characterization

3.1.1 XRD Experiments

Structures of the Pt/Al, Pt/Ba/Al, Ce/Al, Ba/Ce/Al and Pt/Ba/Ce/Al were investigated via XRD. Selected examples from these data sets are presented in the current text, in order to emphasize some of the structural variations among the synthesized materials.

XRD patterns shown in Figure 5 correspond to the 1Pt/Al sample. Two different phases were observed in these XRD patterns which were associated with Pt and γ-Al_2O_3. No other phases were discernible. The peaks at $2\theta = 39.66^o$, 46.72^o and 67.33^o were assigned to the Pt phase while the peaks at $2\theta = 31.21^o$, 32.76^o, 36.72^o, 39.66^o, 45.34^o, 46.12^o, 50.60^o, 60.00^o and 67.33^o were assigned to the γ-Al_2O_3 phase. It is important to note that the Pt diffraction features grew and became sharper at elevated annealing temperatures, indicating crystallographic ordering and sintering of the Pt clusters on the alumina surface. Furthermore, no corundum formation was observed at $T \leq 1273$ K .

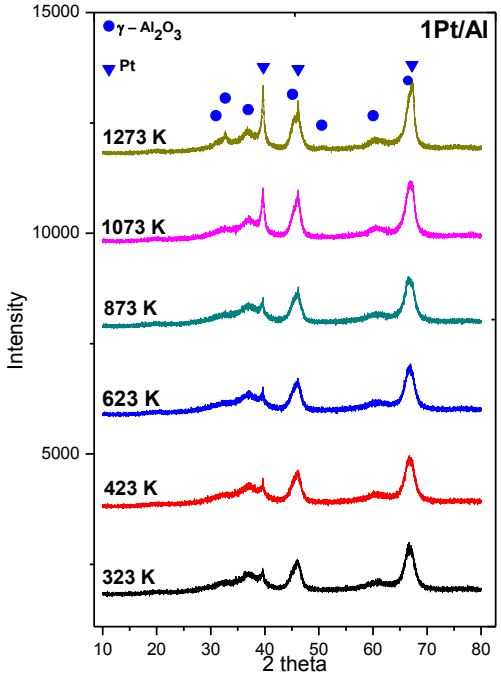

Figure 5: X-ray diffraction patterns of 1Pt/Al after annealing at various temperatures.

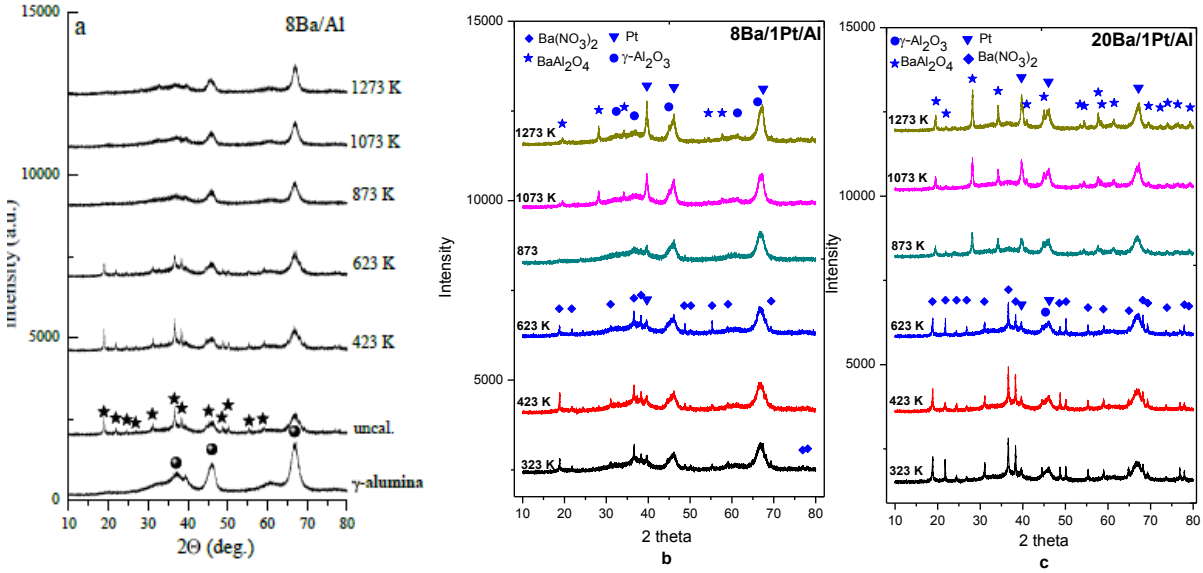

Figure 6: Ex-situ XRD patterns of (a) 8Ba/Al, (b) 8Ba/1Pt/Al, (c) 20Ba/1Pt/Al after annealing at 323 K – 1273 K.

We also examined the 1Pt/Al samples functionalized with different BaO loadings (i.e. 1Pt/8Ba/Al and 1Pt/20Ba/Al) in Figure 6. Unlike the 1Pt/Al sample, we observed two additional sets of signals for the 1Pt/8(20)Ba/Al samples which correspond to $Ba(NO_3)_2$ and $BaAl_2O_4$ phases. At T<823 K, $Ba(NO_3)_2$ peaks were readily observed for both samples. The intensities of these $Ba(NO_3)_2$ features gradually decreased upon further increase in the annealing temperature, eventually vanishing at T> 873 K. As expected, $Ba(NO_3)_2$ features are stronger and sharper for the 1Pt/20Ba/Al sample at all temperatures below 873 K, due to the higher Ba loading in the 1Pt/20Ba/Al sample leading to larger and more ordered $Ba(NO_3)_2$ domains. $BaAl_2O_4$ phase started to appear at T > 873 K. $BaAl_2O_4$ is an undesired phase due to its negative impact on the NO_x trapping ability of the NSR systems [90]. It is worth mentioning that although $BaAl_2O_4$ formation was not visible within 323-1273 K on 8Ba/Al sample, it was clearly visible for 1Pt/8Ba/Al sample at T ≥ 1073 K suggesting that the presence of Pt sites facilitates the diffusion of the BaO domains into the alumina matrix and the formation of the $BaAl_2O_4$ spinnel structure. Formation of the $BaAl_2O_4$ was observed at T ≥ 873 K and also with a larger extent for the 1Pt/20Ba/Al sample due to the increasing Ba loading.

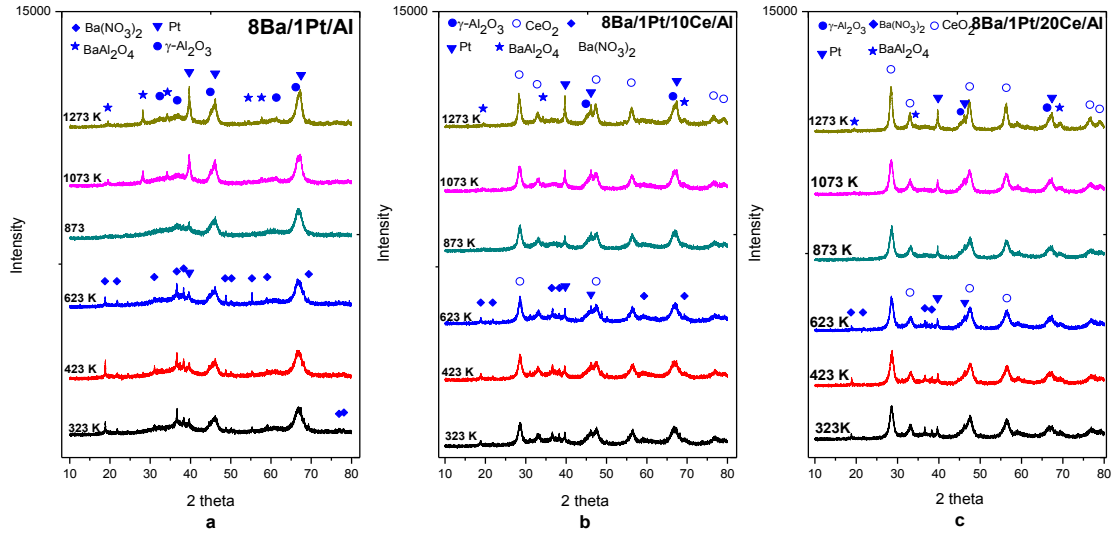

Figure 7: Ex-situ XRD patterns of (a) 8Ba/1Pt/Al, (b) 8Ba/1Pt /10Ce /Al and (c) 8Ba/1Pt/20Ce /Al samples at temperatures between (323 K - 1273 K).

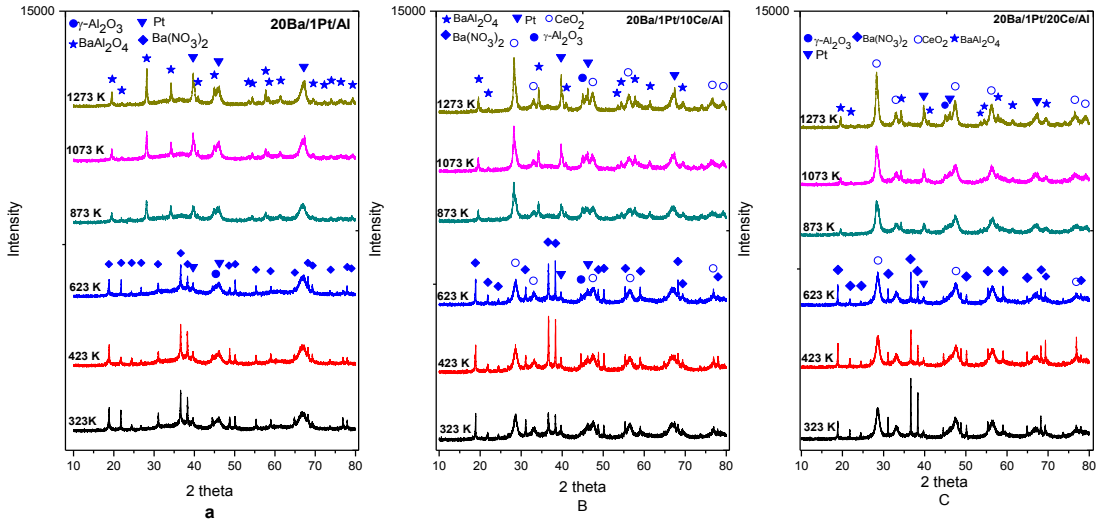

Figure 8: Ex-situ XRD patterns of (a) 20Ba/1Pt/Al, (b) 20Ba/1Pt/10Ce/Al and(c) 20Ba/1Pt//20Ce/Al samples at temperatures between (323 K - 1273 K).

The effect of the ceria loading on the $Pt/BaO/Al_2O_3$ system was investigated via XRD within 323 K to 1273 K, as shown in Figures 7 and 8. γ-Al_2O_3, Pt, $BaAl_2O_4$ and CeO_2 were the main phases that were observed for the Pt/Ce/Ba/Al samples. Two observations are worth emphasizing in Figures 7 and 8. Firstly, it is seen that increasing the Ce loading leads to smaller Pt signal intensities for the Pt/Ce/Ba/Al samples, in comparison to the Pt/Ba/Al counterpart which lacks Ce. This may be explained by the presence of smaller and less ordered Pt clusters in the case of Pt/Ce/Ba/Al, where CeO_2 promoter enhances the Pt dispersion by suppressing the sintering of Pt clusters and limiting their surface diffusion [91]. Secondly, increasing the Ce loading also suppressed the growth of the undesired $BaAl_2O_4$ phase to a certain extent. Although this effect is not very strong, it is still visible. Possible explanation is that some of the CeO_2 domains residing below the BaO clusters provide a diffusion barrier for the BaO phase and hinder the intermixing of the Al_2O_3 support material and the BaO phase, preventing the formation of the $BaAl_2O_4$ structure.

3.1.2 Raman Spectroscopy Experiments

Structural properties of Pt/Al, Pt/Ba/Al, Ce/Al, Ba/Ce/Al and Pt/Ba/Ce/Al were also investigated via Raman spectroscopy. Selected examples from these data sets are presented in the current text in order to emphasize some of the structural variations among the synthesized materials.

Figure 9 presents the Raman spectra for 20Ce/Al and 1Pt/20Ce/Al samples revealing the influence of Pt addition to the (promoted) Ce/Al support material. Raman spectrum of CeO_2 has been previously investigated by Shyu et al. [92], who assigned the 462 cm^{-1} band to the Raman active t_{2g} mode of the fluorite structure. Such a feature is also readily visible in Figure 9a and 9b corresponding to the 20Ce/Al and 1Pt/20Ce/Al samples, respectively. In Figure 9b, additional bands appear at 150, 550, 603, 690 cm^{-1} due to the incorporation of Pt sites onto the 20Ce/Al structure. It is worth mentioning that bands appearing at 550 and 690 cm^{-1} become more intense with increasing ceria loadings (data not shown). These bands can be assigned to the Pt-O-CeO_2 species on the surface which are formed due to the strong metal support interaction (SMSI) between the Pt sites and the underlying CeO_2 domains [93].

A weak feature located at 601cm^{-1} increases upon thermal treatment at 1273 K in Figure 9b. It is known that noble metals can promote reduction of Ce(IV) to Ce(III) [94]. Reduction of Ce sites (accompanied by the oxidation of Pt sites) is favored at higher temperatures as ceria loses some oxide ions from its lattice structure forming a non-stoichiometric CeO_{2-x}. Therefore, the band at 601cm^{-1} in Figure 9b can be associated with intrinsic oxygen vacancies in the defective ceria structure [95]. The feature that is located at 150 cm^{-1} in Figure 9b (1Pt/20Ce/Al) which is not present in Figure 9a (20Ce/Al) is tentatively attributed to the presence of CeO_2 domains that are in the close proximity of the Pt sites or directly linked to the Pt sites.

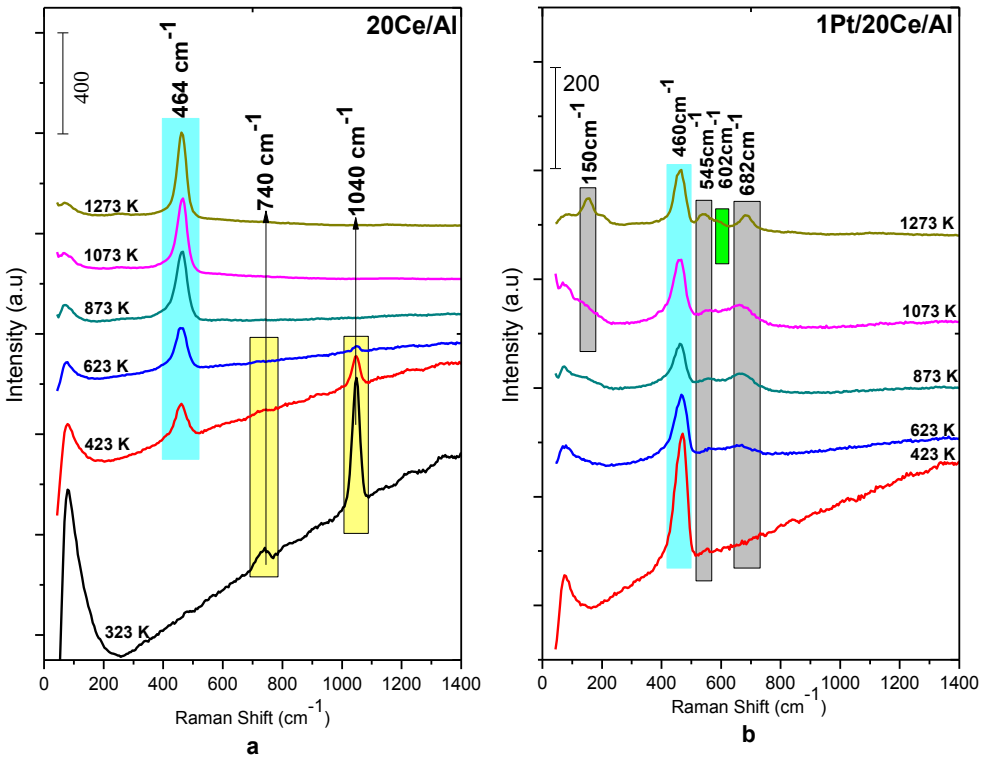

Figure 9: Ex-situ Raman spectra for the (a) 20Ce/Al and (b) 1Pt/20Ce/Al samples that were annealed in Ar(g) at the given temperatures within 323 K – 1273 K.

Another important aspect of Figure 9 is the Raman signals located at 740 and 1040 cm^{-1} which correspond to the bending and the symmetric stretching modes of NO_3^-, respectively [95]. These nitrate groups originate from the ceria precursor used in the synthesis (i.e. $Ce(NO_3)_3.6H_2O$). It is seen in Figure 9a that nitrate decomposition is completed on the 20Ce/Al surface within 873 K >T> 623 K. On the other hand, when the 20Ce/Al system is functionalized with Pt to obtain the 1Pt/20Ce/Al material, nitrate decomposition is completed at 423 K. Thus, it is apparent that the presence of Pt sites facilitates the decomposition of $Ce(NO_3)_3$.

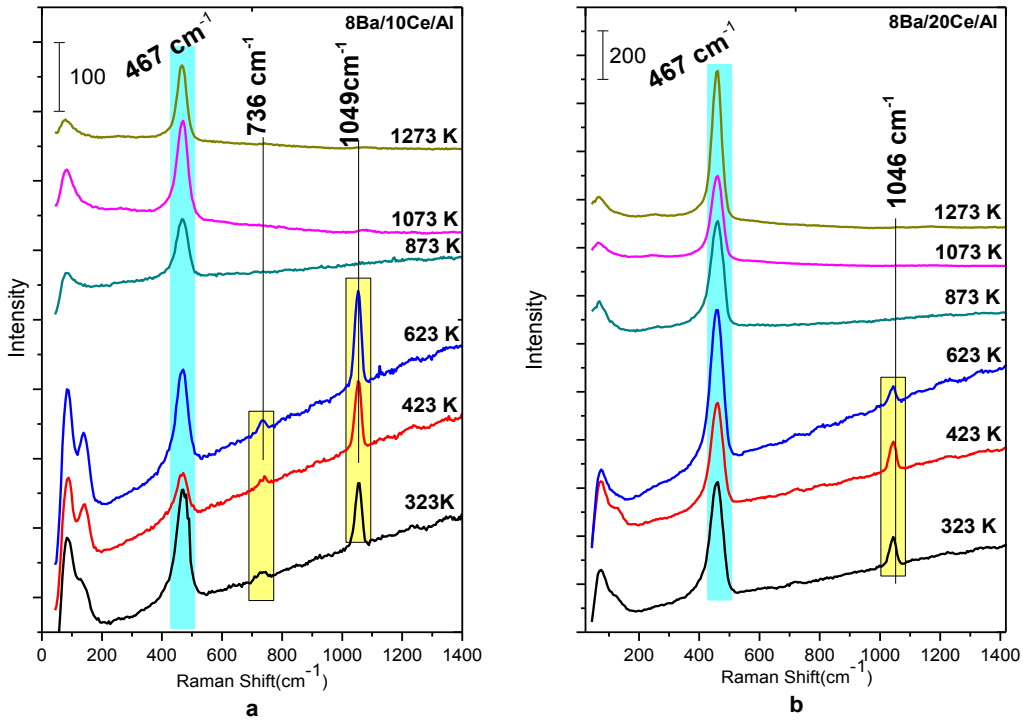

Figure 10: Ex-situ Raman spectra for the (a) 8Ba/10Ce/Al and (b) 8Ba/20Ce/Al samples that were annealed in Ar(g) at the given temperatures within 323 K – 1273 K.

The Raman spectra given in Figure 10 reveal the effect of ceria addition to a conventional NO_x storage material in the form of BaO/Al_2O_3. The feature located at 143 cm^{-1} associated with the lattice phonon excitation of $Ba(NO_3)_2$ indicates the presence of crystalline $Ba(NO_3)_2$ domains. This band is a characteristic feature of all of the synthesized materials where $Ba(NO_3)_2$ was used as a precursor. Increasing the ceria loading causes the band at 467 cm^{-1} to become more visible due to the formation of larger and more ordered CeO_2 domains with increasing Ce loading. It is also visible in Figure 10 that all of the nitrate species coming from the Ce and Ba precursors decompose at T< 873 K from the Ba/Ce/Al samples.

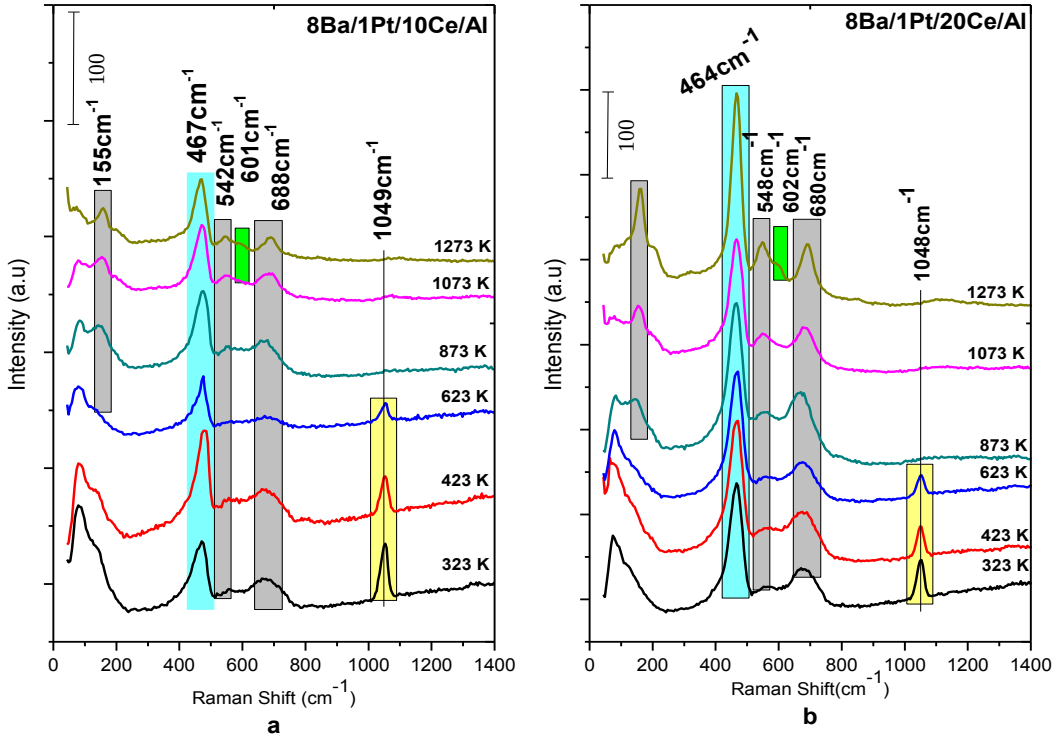

Figure 11: Ex-situ Raman spectra for the (a) 8Ba/1Pt/10Ce/Al and (b) 8Ba/1Pt/20Ce/Al samples that were annealed in Ar(g) at the given temperatures within 323 K – 1273 K.

After having performed Raman analysis of the benchmark samples that are discussed above, similar analysis were also performed for complete ceria promoted NSR catalysts in the form of 1Pt/10(20Ce)/8Ba/Al. Results of such experiments are presented in Figure 11. The bands located at 150, 550, 603, 690 cm^{-1} are observed to increase with increasing ceria loading and increasing annealing temperatures. These bands are attributed to the CeO_2 domains that are directly interacting with the Pt sites. However it is worth emphasizing that, these bands do not uniquely correspond to a single Pt-CeO_2 surface species as the intensity ratio of the 545 cm^{-1} signal to the 682 cm^{-1} signal is not constant and shows some variance at increasing annealing temperatures.

3.1.3 BET

Specific surface areas corresponding to the synthesized samples were found to be significantly affected by the thermal treatments and as an outcome, the SSA values tend to decrease in a monotonic fashion with increasing temperature and increasing both CeO_2 and BaO loading. Such a behavior is rather common for thermal processes leading to sintering. On the other hand, addition of platinum was found to increase the SSA values by a small extent.

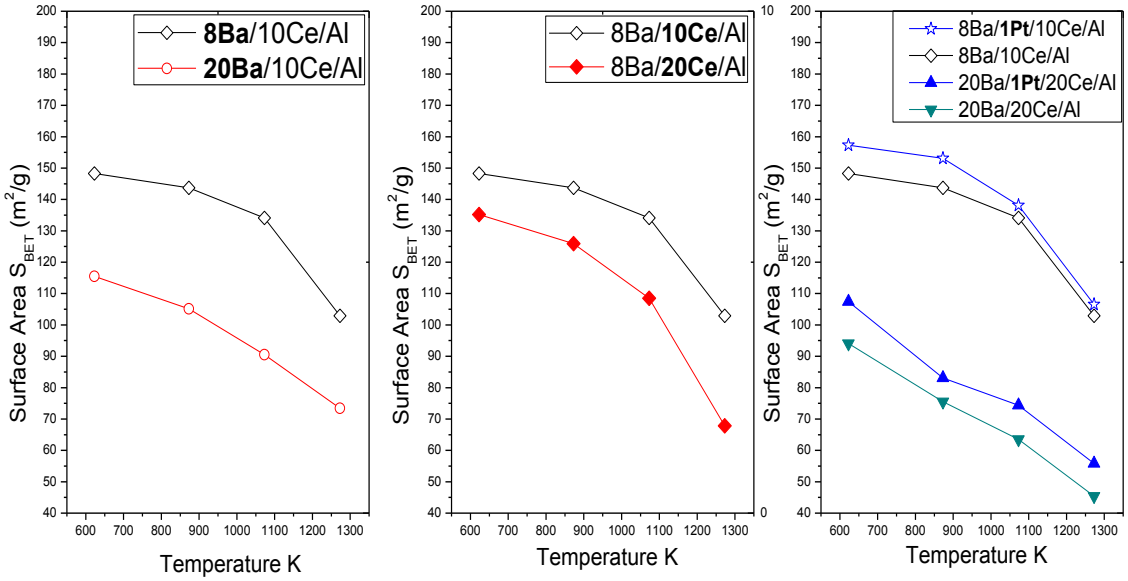

Figure 12: SSA values of the synthesized materials

3.2 FTIR Spectroscopic Analysis of NO_x Adsorption on Synthesized Materials

3.2.1 Stepwise NO_x adsorption on pure γ-Alumina and CeO_2

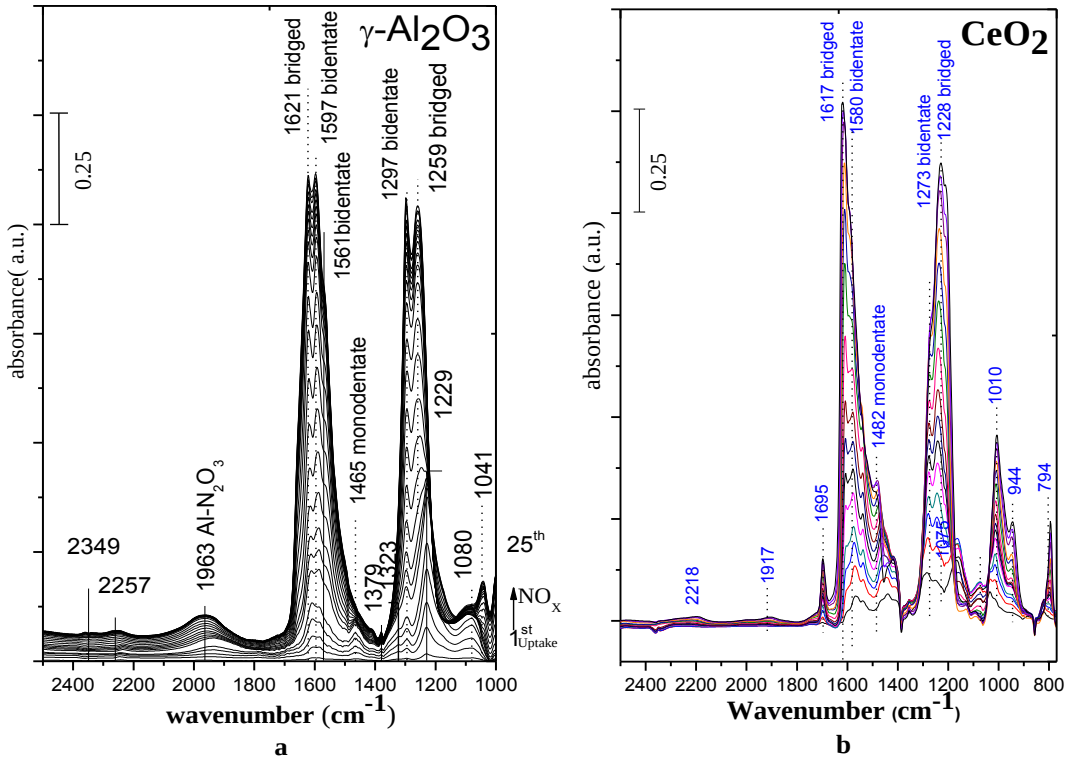

Figure 13: FTIR spectra of stepwise NO_2(g) adsorption on a) γ-Alumina and b) ceria at 323 K.

The FTIR spectra obtained after NO_2 adsorption on pure γ-Al_2O_3 and pure ceria, at 323 K is presented in Figure 13. It is visible in Figure 13a and 13b that the general aspects of the vibrational spectra corresponding to these two surfaces show significant resemblances, revealing similar types of adsorbed NO_x species. Ozensoy et al. [96] has studied NO_2 adsorption mechanism on γ-Al_2O_3 by FTIR spectroscopy. Figure 13 can be interpreted in the light of these former studies. Some of the IR bands given in Figure 13 can be assigned to different types of nitrates formed on the alumina and ceria support such as: bridging (1606–1630 cm^{-1} and 1211–1266 cm^{-1}), bidentate (1571–1612 cm^{-1} and 1249–1293 cm^{-1}), monodentate (1575–1588 and

1292–1297 cm^{-1}), and linear (1479 cm^{-1}) nitrates [97,98]. The band at 1230 cm^{-1} is also assigned to a bridged nitrite species [99].

Bands are also observed near 2250 cm^{-1} and 2220 cm^{-1} for alumina and ceria, respectively. These can be attributed to the weakly adsorbed N_2O species. This feature disappears after outgassing at increasing temperatures [100]. Furthermore, the development of a broad feature in the range of 1920-1980 cm^{-1} can readily be assigned to adsorbed N_2O_3 and/or NO^+ [101].

3.2.2 Ce/Al Binary System

3.2.2.1 Stepwise NO_x adsorption on Ce/Al binary system

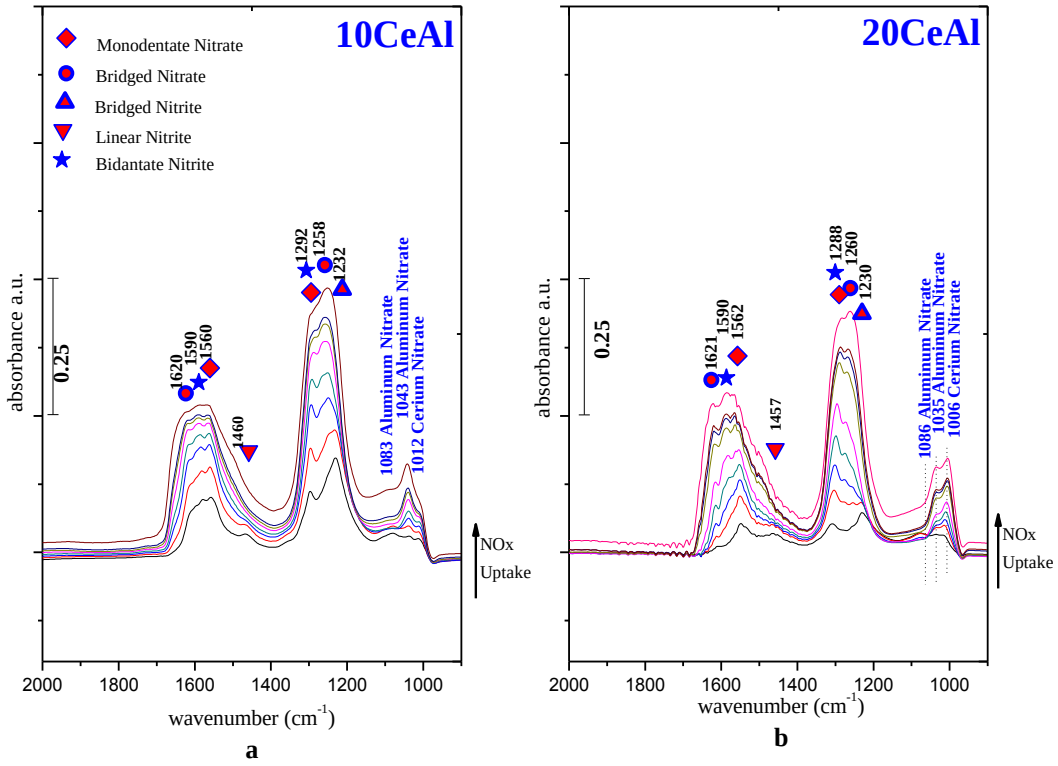

Figure 14: FTIR spectra of stepwise NO_2(g) adsorption on (a) 10Ce/Al and (b) 20Ce/Al at 323 K.

NO_2 uptake properties of ceria promoted alumina support materials (i.e. 10Ce/Al and 20Ce/Al) are also investigated in stepwise NO_2 adsorption experiments via FTIR spectroscopy at 323 K. These results are presented in Figure 14. It is apparent that increasing the ceria loading from w%10 to w%20 does not have a significant influence on neither types of the adsorbed NO_x species nor their relative surface coverages. During the very early stages of the NO_2(g) uptake, the most dominant signal is located 1230 cm^{-1} which is associated with the bridging nitrites [99]. Further increase in the NO_2 exposure leads to the oxidation of these nitrite species to form various types of nitrates as a result of the disproportionation of NO_2 on the surface.

3.2.2.2 Effect of Pt on the NO_x uptake properties of Ce/Al binary system

After having investigated the NO_x uptake properties of the simple Al_2O_3 and CeO_2 support materials as well as promoted support materials in the form of Ce/Al, influence of the Pt sites on the NO_x uptake properties of promoted Ce/Al support materials were also studied via FTIR spectroscopy. Results of these investigations are shown in Figure 15.

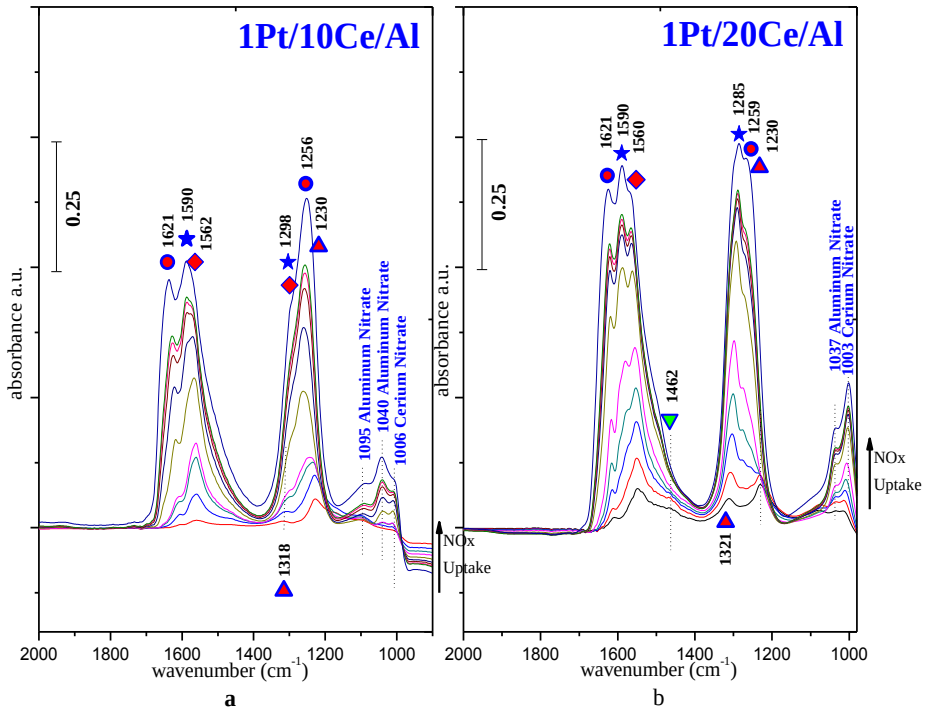

Figure 15: FTIR spectra of stepwise NO_2(g) adsorption on (a) Pt/10Ce/Al and (b)1Pt/20Ce/Al at 323 K.

Comparison of Figure 14 and 15 reveals that upon addition of Pt (Figure 15), an enhancement in the intensities of the bidentate and bridging nitrate signals are apparent while the intensities of the monodentate nitrates decrease to a certain extent. Furthermore, bidentate and bridging nitrate signals seem to be better resolved in Figure 15. In addition , increasing Ce loading in the Ce/Al (Figure 16) and Pt/Ce/Al (Figure 15) systems have a discernible influence on the nitrate band intensities, where the IR signal intensities for the nitrate species increase for 20 wt% Ce loading. Although this effect is less pronounced in the case of 10(20)Ce/Al, it is more readily visible in 1Pt/10(20)Ce/Al.

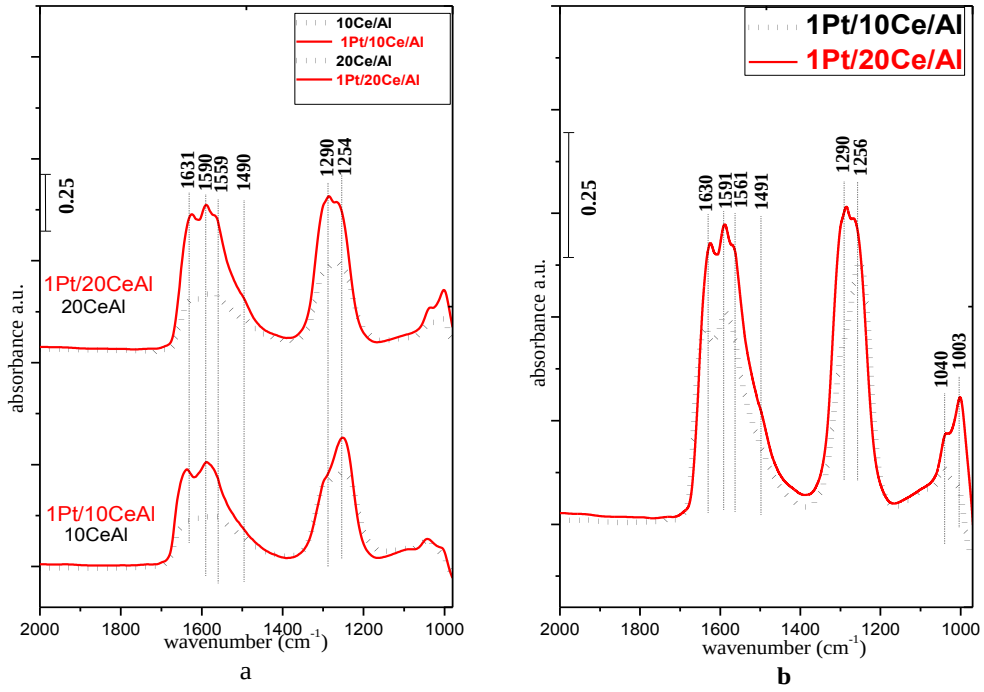

Figure 16: A comparative analysis of the FTIR spectra corresponding to stepwise NO_2(g) adsorption on Ce/Al and Pt/Ce/Al systems at 323 K, revealing the influence of Pt.

In order to clearly demonstrate the influence of the Pt sites on the total NO_x uptake capacity of the promoted Ce/Al support materials, FTIR data given in Figures 16 and 15 are analyzed in a comparative fashion as shown in Figure 16. Figure 16a, reveals that Pt addition to the promoted Ce/Al support material results in a significant enhancement of the NO_x uptake capacity where this enhancement is more discernible for the 20Ce/Al case. The increase in NO_x uptake capacity are also in line with the presence of the bands at 550 and 690 cm^{-1} in the corresponding Raman spectra of these materials suggesting the existence of Pt-O-CeO_2 surface species and a strong metal support interaction between Pt and CeO_2 [93]. Thus, it is apparent that these Pt sites which are in close proximity of the CeO_2 domains catalyze the nitrate formation process and increase the quantity of the nitrate species stored by the Pt/Ce/Al system. As mentioned above, although Ce loading has a minor influence on the NO_x uptake capacity in the case of Ce/Al, NO_x uptake capacity becomes quite sensitive to Ce loading in the case of Pt/Ce/Al system indicating that the Pt sites can readily activate some of the CeO_2 domains on the surface which are not active for NO_x uptake in the absence of Pt sites. The catalytic function of the Pt sites in the nitrate formation process can be associated with the facile NO_2 activation on the Pt surface yielding atomic oxygen species which readily spill over from the Pt surface to the neighboring CeO_2 and Al_2O_3 sites enabling the nitrate formation on the oxide domains. In other words, Pt sites may function as atomic oxygen transporters. Alternatively, nitrate species may also be forming directly on the Pt sites followed by a facile spill-over towards the alumina and ceria domains.

3.2.2.3 Effect of Pt on the Thermal Stability of Adsorbed NO_x on the Ce/Al Binary System

Thermal stability of the adsorbed NO_x species were also investigated via TPD technique. After having studied the chemical nature and the vibrational properties of the adsorbed NO_x species on the standard support materials (i.e. γ-Al_2O_3 and CeO_2), promoted support materials (i.e. Ce/Al) and their Pt functionalized forms, we have also investigated their TPD profiles after NO_2 adsorption. Figure 17 shows such TPD experiments obtained after saturating the given surfaces with NO_2 at 323 K as described above.

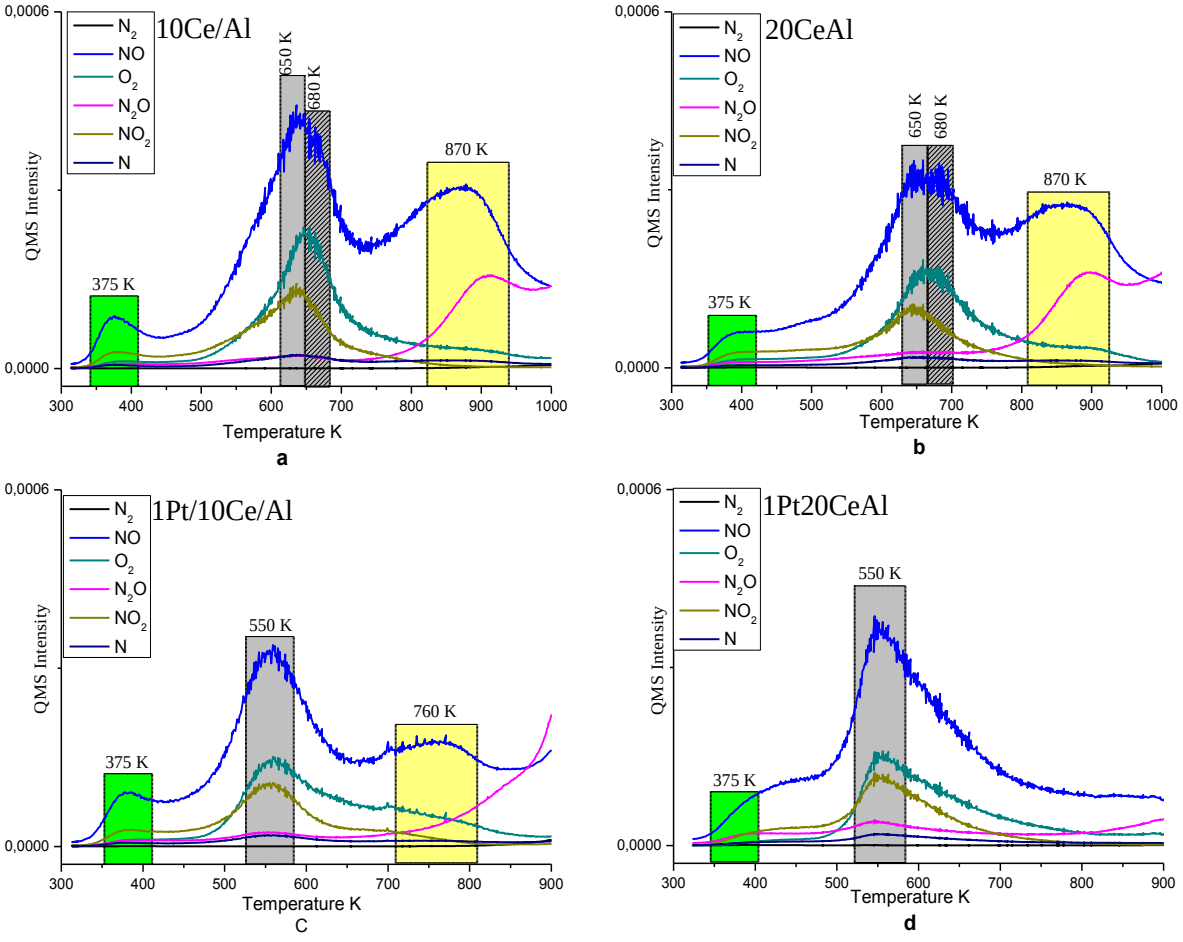

Figure 17: TPD profiles obtained after NO_2 saturation at 323 K of (a) 10Ce/Al, (b) 20Ce/Al, (c) 1Pt/10Ce/Al, (d) 1Pt/20Ce/Al.

We previously investigated the thermal desorption profiles of γ-Al_2O_3 surface after saturation with NO_2 at 323 K (data not shown) which yielded two major NO_x desorption peaks at 389 K and 625 K [109]. The first NO_x desorption has been assigned to weakly bound N_2O_3/NO^+ or monodentate nitrate species [101-103]. The second feature, which was also the most prominent desorption signal, has been attributed to bridging and bidentate nitrates [102,103]. TPD profiles in Figures 17a and 17b demonstrate a major desorption band which has two overlapping desorption signals located at 630 K and 680 K. The former signal at 630 K can be assigned to desorption of bridging and bidentate nitrates from γ-Al_2O_3 surface [104]. The latter signal at 680 K, which becomes better resolved upon increasing Ce loading, can be tentatively assigned to the desorption of slightly more stable surface nitrates bound to CeO_2. Desorption feature at 870 K is associated with the decomposition of bulk and/or ionic nitrates resulting from $Ce(NO_3)_3$ and/or $Ce(NO_3)_4$ with a characteristic N_2O desorption accompanying the NO and O_2 desorption signals. The most striking aspect of the TPD profiles given in Figure 17 is seen in Figures 17c and 17d corresponding to the Pt containing 1Pt/10(20)Ce/Al samples. It is evident that the addition of Pt to the Ce/Al system has a very drastic impact on the thermal stability of the bulk cerium nitrate species (i.e. desorption signals located at 760 - 870 K) indicating a strong interaction between the Pt sites and the underlying $CeO_2/Ce(NO_3)_x$ system, in very good agreement with the current Raman spectroscopic, XRD and FTIR results, indicating that Pt sites catalyze the nitrate decomposition. Such a catalytic behavior of the Pt sites is not limited to the Ce sites and was also observed for the nitrates on the γ-Al_2O_3 sites which seem to be desorbing at temperatures that are about 100 K lower than that of the Ce/Al system (650 K vs 550 K). Furthermore, the catalytic effect of the Pt sites also seem to be altering the nitrate decomposition mechanism particularly for the bulk cerium nitrates as the characteristic N_2O desorption signal observed for these species in case of 10(20)Ce/Al samples (Figures 17a and 17b) is lost after the addition of Pt (Figures 17c and 17d).

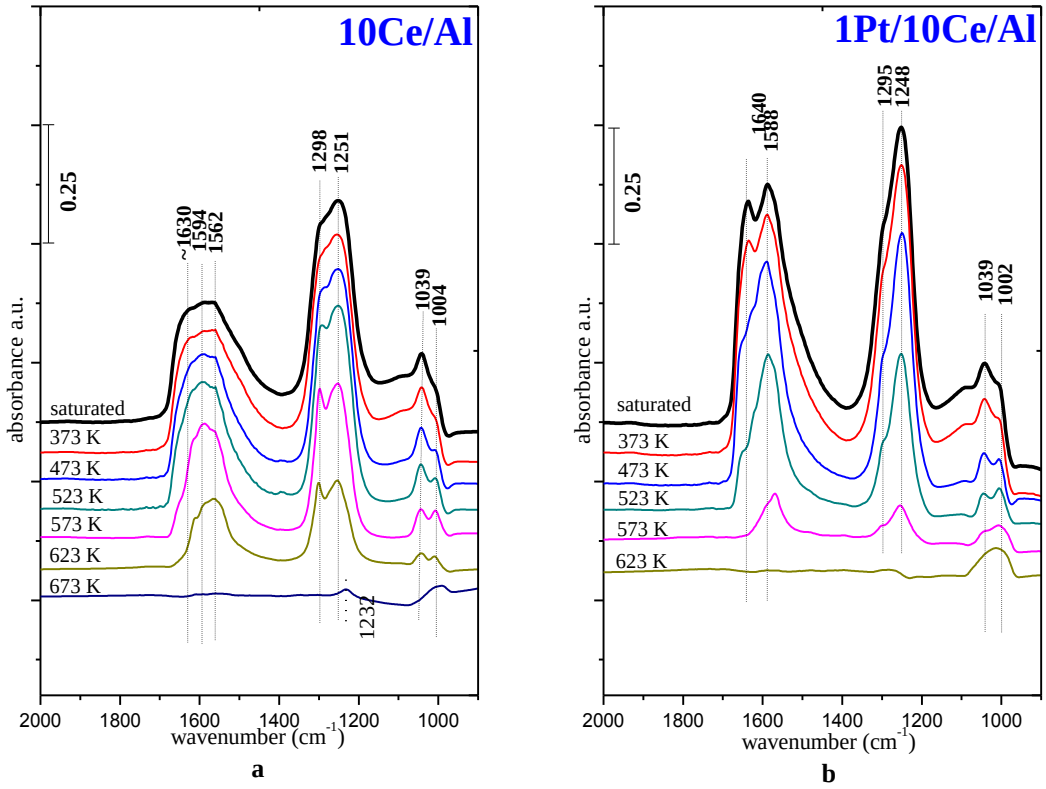

Figure 18: Temperature dependent FTIR spectra for NO_2(g) saturated (a) 10Ce/Al, (b)1Pt/10Ce/Al samples between 323 K – 673 K.

Thermal decomposition of the adsorbed NO_x species were also investigated via FTIR spectroscopy and these results were analyzed in a complementary fashion to the corresponding TPD experiments discussed above. Figure 18 shows some of the selected data corresponding to such FTIR experiments emphasizing the influence of Pt addition on the thermal stability of the adsorbed NO_x species on the Ce/Al system. Examining Figure 18a reveals that the complete removal of the nitrate species occurred at a lower temperature in the presence of Pt sites. Furthermore, it is also apparent in Figure 18 that the Pt addition has a more direct influence on the bridging nitrate species (1620 cm^{-1}) where these species seem to be preferentially destabilized/decomposed upon Pt addition.

3.2.3 Ba/Ce/Al Ternary System

3.2.3.1 Stepwise NO_x Adsorption on the Ba/Ce/Al Ternary System

A new ternary NO_x storage system in the form of Ba/Ce/Al was also designed in the current work and the interaction of the NO_x species with the synthesized ternary NO_x storage materials was investigated. Four different ternary support oxide were prepared with different baria (w%8 and w%20) and ceria (w%10 and w%20) loadings.

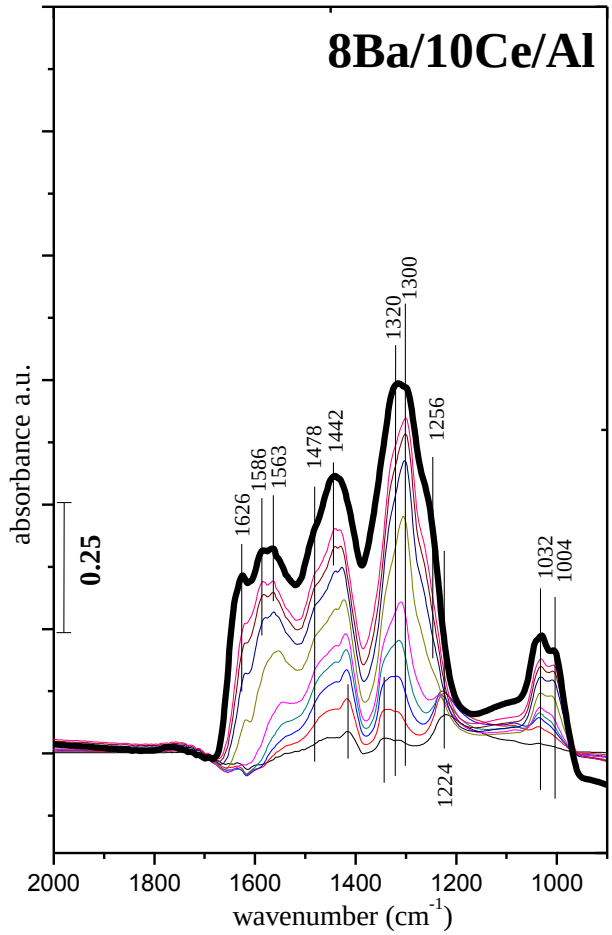

Figure 19: FTIR spectra corresponding to stepwise NO_2(g) adsorption on a 8Ba/10Ce/Al surface at 323 K.

NO_2 adsorption on 8Ba/Al sample has been thoroughly analyzed in the former studies of our research group as well as others in the literature [105-110]. Thus, NO_2 adsorption behavior of the 8Ba/Al sample will not be discussed in detail here. However, it is worth mentioning that NO_2 adsorption experiments on the 8Ba/Al system via FTIR reveals the formation of nitrites during the initial stages which is followed by the formation of surface and bulk nitrates on the BaO sites as well as surface nitrates on the alumina sites in the later stages of the adsorption

process. A minor amount of weakly bound N_2O_3/NO^+ species were also observed on the 8Ba/Al system. Similar stepwise NO_2 adsorption experiments were also performed via FTIR on the on the 8Ba/10Ce/Al surface (Figure 19). Initial doses NO_2 led to dominant features at 1225 and 1478 cm^{-1} which are assigned to nitrite species on the BaO sites and linear nitrites on the support surface, respectively [111-114]. Further doses of NO_2 resulted in the oxidation of the surface nitrites into nitrate species which is evident by the additional asymmetric stretching bands at 1300, 1565, 1585 cm^{-1} that can be attributed to bidentate surface nitrates. The shoulders at 1320 and 1440 cm^{-1} can be assigned to bulk barium nitrates . Kwak and Szanyi reported that 8 wt% Ba loading is not enough to cover all of the support surface [105,106]. Along these lines, the shoulders at 1630 and 1256 cm^{-1} can be attributed to the presence of bidentate nitrates on the support surface. Weak features at 1003, 1032 and 1041 cm^{-1} are also associated with the symmetric stretching modes of nitrate groups.

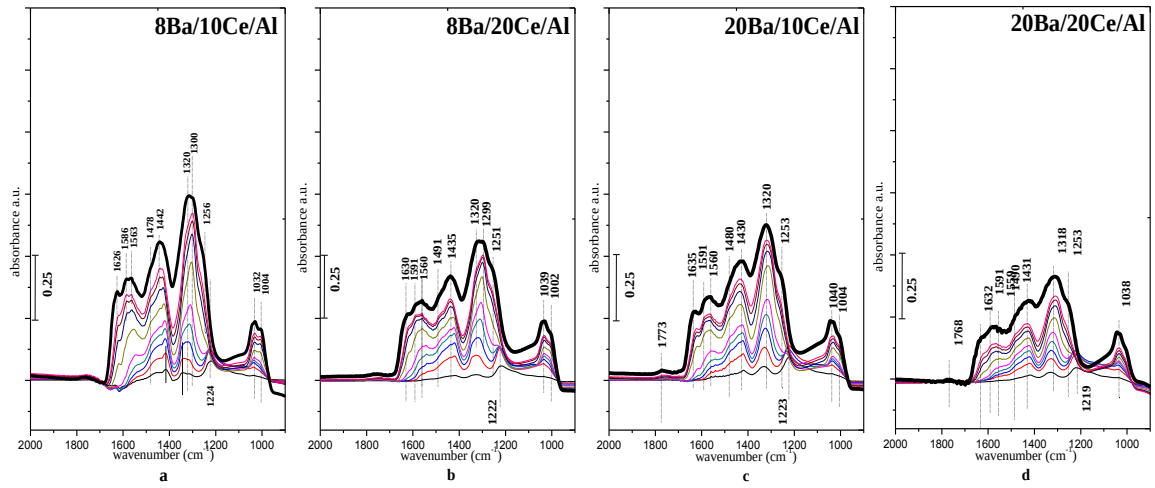

Figure 20: FTIR spectra corresponding to stepwise NO_2(g) adsorption at 323 K on (a) 8Ba/10Ce/Al, (b) 8Ba/20Ce/Al, (c) 20Ba/10Ce/Al, (d)20Ba/20Ce/Al.

Similar NO_2 uptake experiments were also performed with other Ba/Ce/Al systems with varying Ba and Ce loadings as shown in Figure 20. General characteristics of the spectral line shapes are very similar for the samples given in Figure 20. However, overall intensities of the NO_x signals show some variance as a function of composition. It is seen that 8Ba/10Ce/Al sample has the highest NO_x signals (Figure 20a). Thus, it can be argued that 8 wt% Ba loading is enough for wetting a significant fraction of the CeO_2/Al_2O_3 support surface and disperse BaO sites in an efficient manner for the NO_x uptake. However, NO_x signals were found to be relatively attenuated for all other samples given in Figure 20. This may be associated with the decreasing specific surface area values with increasing Ba and Ce loadings, as discussed in Section 3.1.3. Furthermore, formation of the undesired $BaAl_2O_4$ phase for the higher Ba loadings which was verified by the XRD experiments (data not shown) may also play a role in the decreasing NO_x uptake of the 20Ba/10(20)Ce/Al samples.

3.2.3.2 Influence of Pt on the NO_x Uptake Properties of the Ce/Ba/Al Ternary System

FTIR spectra corresponding to the NO_2 adsorption on the synthesized Pt/Ba/Ce/Al samples at 323K are shown in Figure 21. The types of the nitrate species generated on the surface show significant resemblance to that of the Pt-free samples given in Figure 20. On the other hand, 1Pt/8Ba/10Ce/Al showed the largest variation in its NO_x related IR bands. These changes are highlighted in a more apparent manner in Figure 20 which compares the FTIR spectra for these surfaces after NO_x saturation at 323 K.

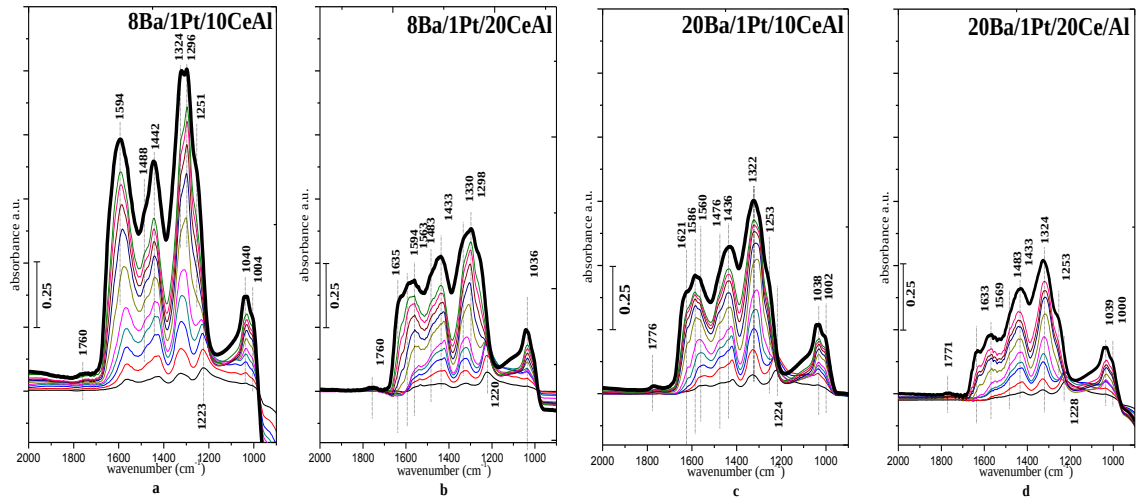

Figure 21: FTIR spectra of stepwise NO_2(g) adsorption on a) 8Ba/1Pt10Ce/Al b) 8Ba/1Pt//20Ce/Al c) 20Ba/1Pt//10Ce/Al d) 20Ba/1Pt/20Ce/Al at 323 K.

Figure 22 implies that Pt addition to the Ba/Ce/Al system increases the NO_x storage capacity of all of the investigated samples. The reasons behind the enhancement of the NO_x uptake due to Pt addition can be envisioned in the way it was proposed for the Pt/Ce/Al system which was discussed in Section 3.2.2.2.

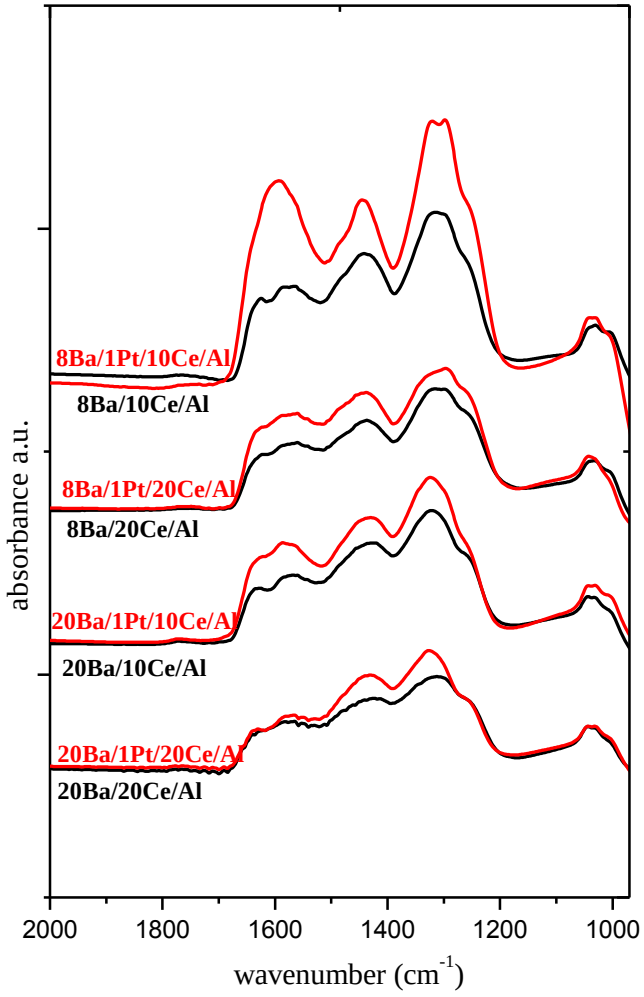

Figure 22: FTIR spectra obtained after NO_2(g) saturation on Pt-free Ba/Ce/Al (black line) and Pt-containing Pt/Ba/Ce/Al (red line) samples at 323 K.

3.2.3.3 Thermal Behavior of NO_x Species on the Ba/Ce/Al Ternary System

Thermal stabilities of the adsorbed NO_x species on the Ba/Ce/Al system were also investigated via FTIR spectroscopy as shown in Figures 23 and 24. It is apparent that the nitrate decomposition behavior of the 10(20)Ce/8Ba/Al samples at elevated temperatures (Figure 23) shows significant differences to that of the 10(20)Ce/20Ba/Al samples (Figure 24). On the 10(20)Ce/8Ba/Al samples (Figure 23), within 323 – 623 K, the IR signals corresponding to the surface nitrates on the BaO sites (1590 cm^{-1}) stayed rather constant while bulk barium/cerium nitrates (1420 cm^{-1}) and the surface nitrates on the alumina and ceria sites (1620 cm^{-1}) were constantly consumed. It is likely that under these conditions, nitrates that are decomposing from the surface of the small Ba clusters are constantly replenished by the bulk barium/cerium nitrates, maintaining a rather invariant coverage for the surface barium nitrates. Above 623 K, due to the constantly depleting bulk nitrates, surface barium nitrates cannot be replenished effectively anymore and thus, both bulk and surface barium nitrates start to vanish in a simultaneous fashion.

On the other hand a different nitrate decomposition behavior was observed for the 10(20)Ce/20Ba/Al samples (Figure 24) where nitrates on the alumina and ceria sites (1620 cm^{-1}) vanished first, followed by the surface barium sulfate species (1590 cm^{-1}) while bulk barium/cerium nitrates (1420 cm^{-1}) decomposed at higher temperatures. This can be explained by the lack of small BaO clusters that are in close proximity of the large 3-D BaO nanoparticles and thus replenishing the surface barium nitrates (i.e. diffusion of the nitrates from the bulk of the Ba/Ce domains to the surface and then spilling over towards neighboring small BaO clusters) is less likely.

Another important aspect of Figure 24 is the observation that increasing CeO_2 loading decreases the nitrate decomposition temperatures to lower values. It is worth mentioning that the thermal NO_x decomposition/release trends for the 1Pt/8(20)Ba/10(20)Ce/Al samples were also studied in an analogous way via FTIR spectroscopy (data not shown) and the observed behavior was quite similar to that of Figure 24. The only important difference in the case of 1Pt/8(20)Ba/10(20)Ce/Al samples was the observation that all of the decomposition temperatures were shifted

to lower temperatures in comparison to the 8(20)Ba/10(20)Ce/Al samples which lack Pt.

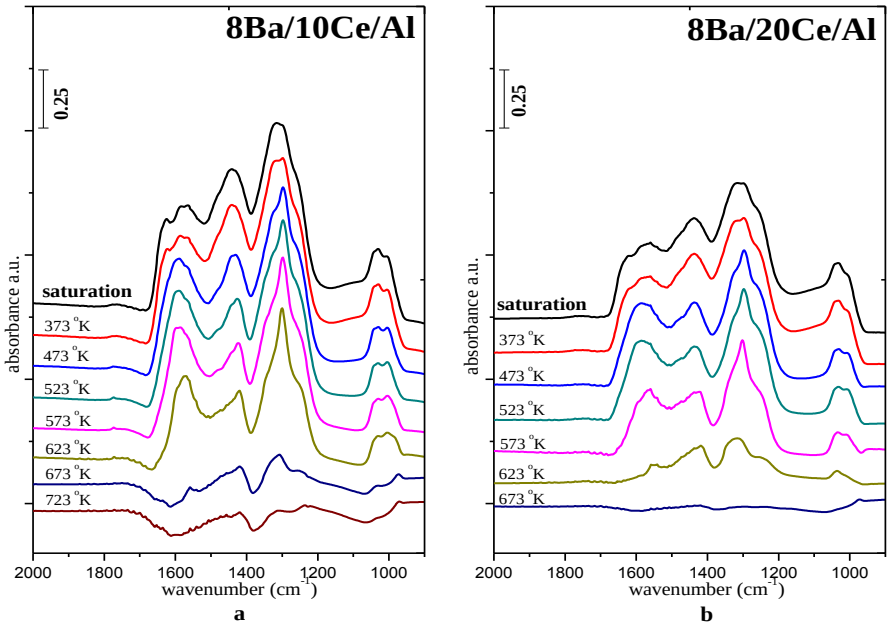

Figure 23: FTIR spectra of stepwise heating on a) 8Ba/10Ce/Al b) 8Ba/20Ce/Al in temperature range between 323 K-723 K.

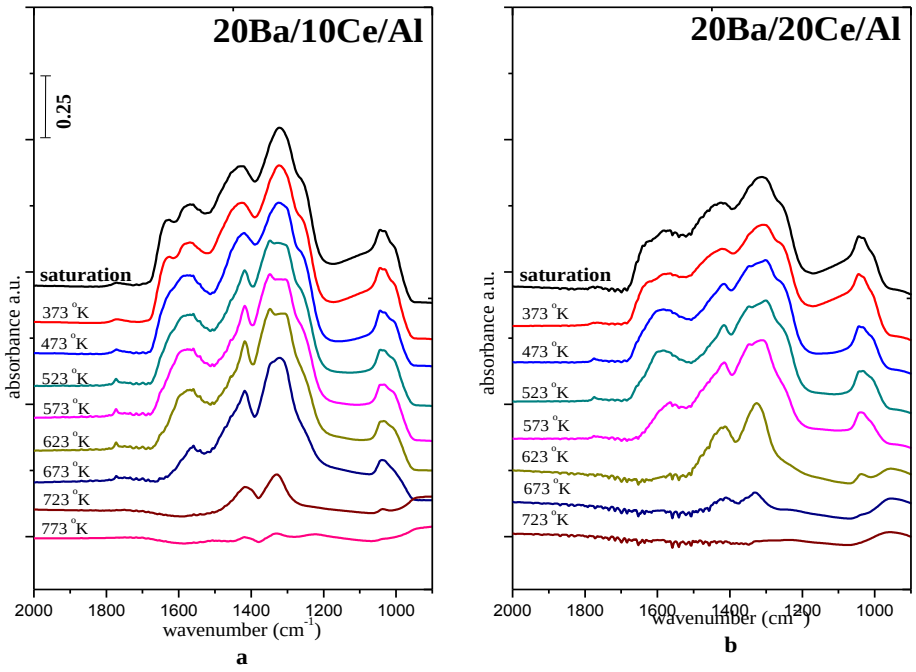

Figure 24: FTIR spectra of stepwise heating on a) 20Ba/10Ce/Al b) 20Ba/20Ce/Al in temperature range between 323 K-723 K.

FTIR experiments given in Figure 23 and 24 revealing the thermal nitrate decomposition from the Ba/Ce/Al samples were also supported by the TPD experiments obtained after saturating 8(20)Ba/10(20)Ce/Al and 1Pt/8(20)Ba/10(20)Ce/Al samples with NO_2 at 323 K. Selected examples from these TPD experiments are given in Figure 25. The desorption signals given in Figure 25 can be assigned in the following manner: for the Ba/Ce/Al samples the desorption signal at c.a. 675 K is associated with surface nitrates on the alumina, ceria and baria domains, the desorption signal at 685-750 K is associated with bulk barium nitrates while the desorption signal at 900 K (accompanied by a characteristic N_2O desorption signal) is associated with the bulk cerium nitrates. In the light of the discussion regarding the FTIR data given in Figure 24, it can be argued that the smaller bulk barium nitrate desorption signal for the 8Ba/10Ce/Al sample (Figure 25a) is due to the diffusion of nitrates from the bulk of the barium domains towards the surface (which is not the case for the 10(20)Ce/20Ba/Al samples). For the Pt containing samples (Figures 25c-25e), it was observed that all of the nitrate desorption signals (except bulk cerium nitrate and N_2O_3/NO^+ desorption signals) were shifted to lower temperatures by 50-100 K, revealing the catalytic influence of the Pt sites in the NO_x release process.

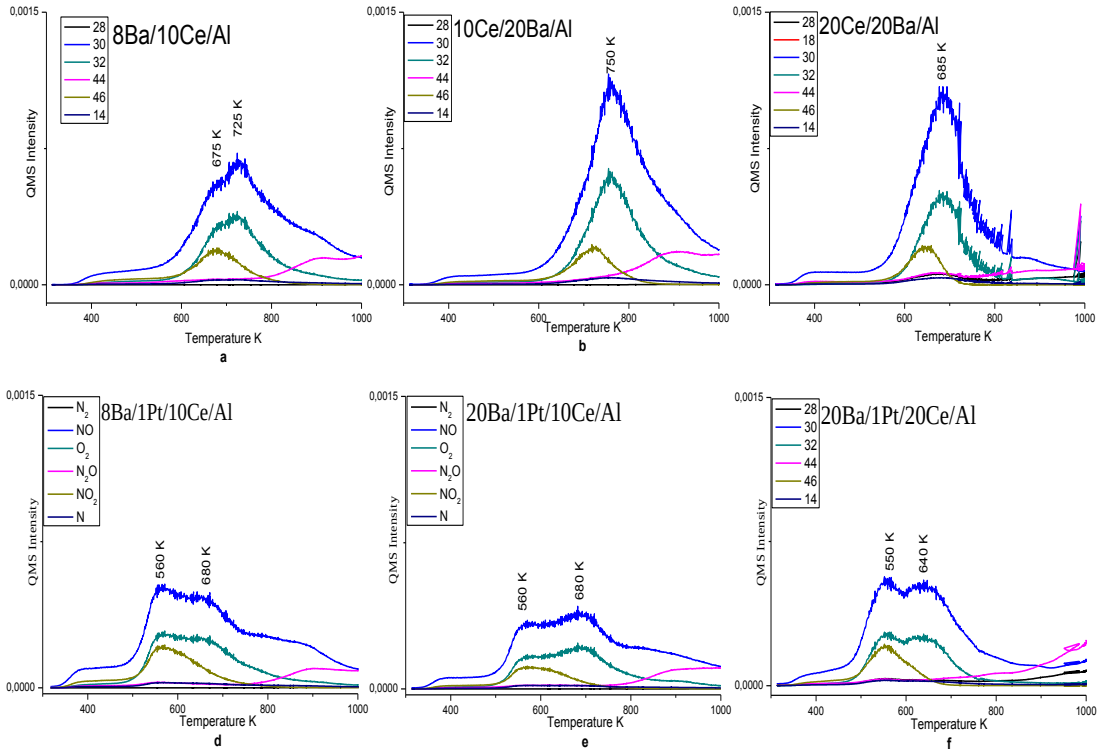

Figure 25: TPD profiles obtained after saturating on a) 8Ba/10Ce/Al b)20Ba/10Ce/Al c) 20Ba/20Ce/Al d) 8Ba/1Pt/10Ce/Al e) 20Ba/1Pt/10Ce/Al f) 20Ba/1Pt/20Ce/Al

3.3 FTIR Spectroscopic Analysis of SO_x Uptake of the Synthesized Materials

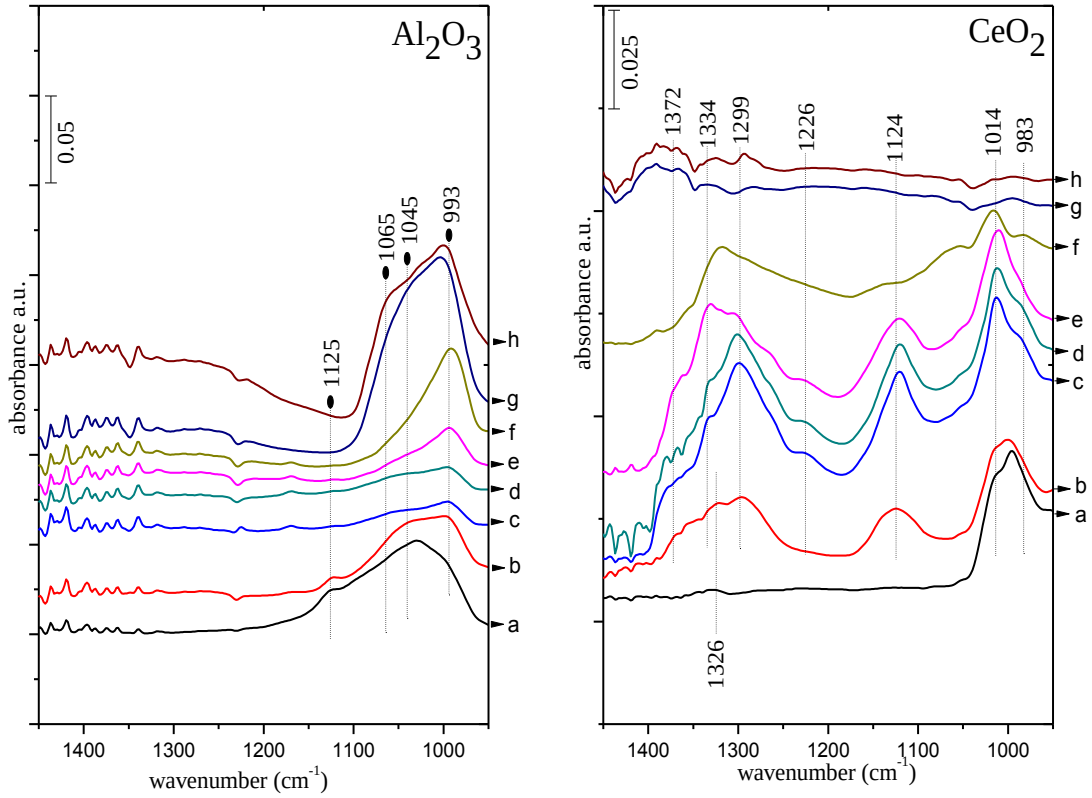

Figure 26: FTIR spectra for SO_2 (g) + O_2 (g) (SO_2:O_2, 0.1:1) co-adsorption on γ-Al_2O_3 and CeO_2. (a) After 10 min exposure to SO_2 (g) + O_2 (g) at 323 K (spectrum was obtained in the presence of the gas mixture), after flashing the sample to (b) 473 K, (c) 673 K in SO_2 + O_2 and cooling to 323 K (spectrum was obtained in the presence of the gas mixture), (d) after SO_2 (g) + O_2 (g) mixture evacuated ($P_{reactor}$ ~1×10-3 Torr) , after flashing the sample to (e) 473 K, (f) 673 K, (g) 873 K and (h) 1073 K in vacuum ($P_{reactor}$ < 1×10^{-3} Torr) and cooling to 323 K.

The adsorption of SO_2 (g) + O_2 (g) on the γ-Al_2O_3 and CeO_2 surface is represented in Figure 26. A large number of former studies exist on the interaction of sulfur species on the γ- Al_2O_3 surface [86, 115-117]. Our current FTIR data (Figure 26, left panel) reveal a major broad band at 1065, 1030 and 993 cm^{-1} as well as a poorly defined additional feature at 1125 cm^{-1} after SO_2+O_2 adsorption at 323 K for 10 min. It is important to mention that the well-known vibrational band located ~

1360cm^{-1} which is attributed to surface aluminum sulfate was not observed in Figure 26a. This due to the relatively short SO_x exposure duration used in the current study. Kylhammar et al. [86] reported that the formation of the feature at 1360 cm^{-1} started to grow when the duration of the SO_x exposure was longer than 60 min. The shoulder located at 1125 cm^{-1} in Figure 26 which disappeared at 473 K can be attributed to the symmetric stretching mode of weakly adsorbed molecular SO_2 species [115-117]. The strong bands observed at 1065 and 1045 cm^{-1} (Figure 26, left panel) are attributed to tri-coordinated sulfite species which became less pronounced upon increasing temperature up to 673K in the SO_2 (g) + O_2 (g) gas mixture. However, these sulfite species regain their intensities upon annealing at T > 673 K in vacuum.

The major vibrational bands obtained for the analogous experiments on ceria (Figure 26, right panel) revealed bands at 1014, 993 and 983 cm^{-1} after SO_x exposure at 323 K. Upon increasing the temperature to 473 K, new bands appeared at 1124, 1226, 1300 and 1372 cm^{-1}. Waqif et al. [70] previously assigned vibrational bands between 1400-1340cm-1 and bands below 1050 cm^{-1} to surface sulfates and weakly bound surface sulfites, respectively. Low frequency band at 983 cm^{-1} which appeared after 473 K annealing indicates the formation of surface cerium sulfate. Two different broad features between 1220-1150 cm^{-1} and 1200-1060 cm^{-1} can be assigned to bulk type of sulfates on ceria [70]. Bulk type of sulfate species grew in intensity with increasing the annealing temperature to 673 K in the presence of SO_2 (g) + O_2 (g) mixture. However, heating in vacuum at 673 K, caused bulk sulfates to decompose. The minor band around ~1326 cm^{-1} which disappeared after annealing at 473 K has been previously attributed to weakly bound physisorbed SO_x species. Most of the sulfite and sulfate species which were formed within the temperature range between 323-673K left the ceria surface at 873 K. However, even after annealing at 1073 K in vacuum, some of the sulfur species remained on the surface.

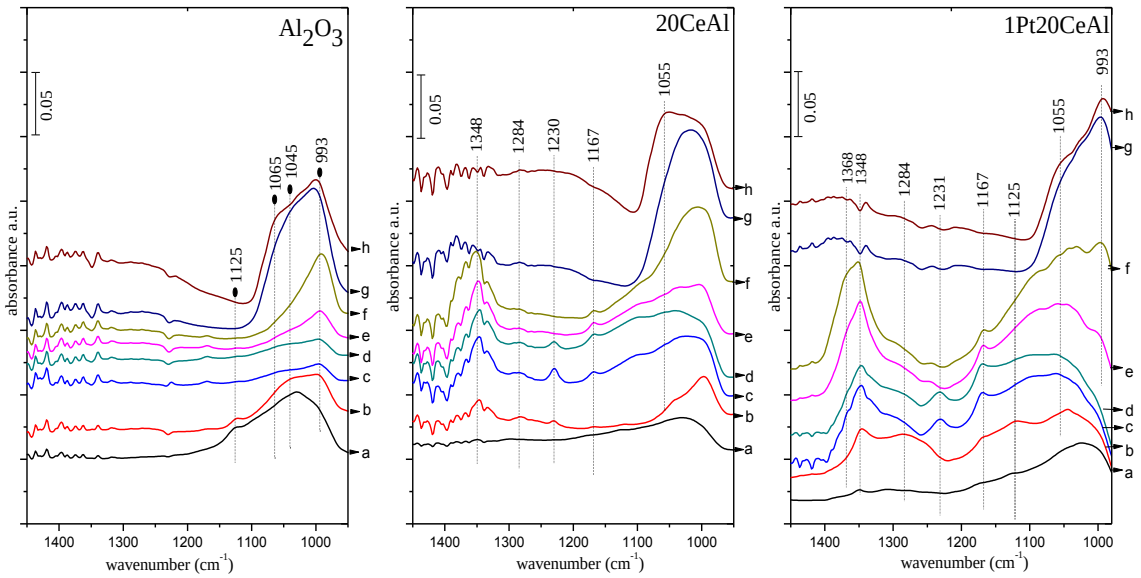

Figure 27: FTIR spectra for SO_2 (g) + O_2 (g) (SO_2:O_2, 0.1:1) co-adsorption on γ-Al_2O_3, 20Ce/Al and 1Pt/20Ce/Al. a) After 10 min exposure to SO_2 (g) + O_2 (g) at 323 K (spectrum was obtained in the presence of the gas mixture), b) after flashing the sample to b) 473 K c) 673 K in SO_2 + O_2 and cooling to 323 K (spectrum was obtained in the presence of the gas mixture), d) after SO_2 (g) + O_2 (g) mixture evacuated ($P_{reactor}$ ~1×10-3 Torr) , after flashing the sample to e) 473K f) 673K g) 873K and h)1073K in vacuum ($P_{reactor} < 1\times10^{-3}$ Torr) and cooling to 323 K.

Figure 27 compares the FTIR spectra corresponding to pure alumina, 20Ce/Al and 1Pt/20Ce/Al systems. Ceria promotion of the simple alumina support material led to the formation of a vibrational band around ~ 1350 cm^{-1} for the 20Ce/Al sample, which is assigned to surface sulfates. This can be explained by the facile SO_x oxidation due to the oxygen storage/transport capability of the ceria lattice in the 20Ce/Al system. This feature becomes even more pronounced in the presence of Pt. As discussed above, Pt addition leads to formation of Pt-O-CeO_2 species which may facilitate the oxygen transfer from the ceria lattice to the SO_x species. Pt species can also directly activate O_2 and enhance the SO_x oxidation.

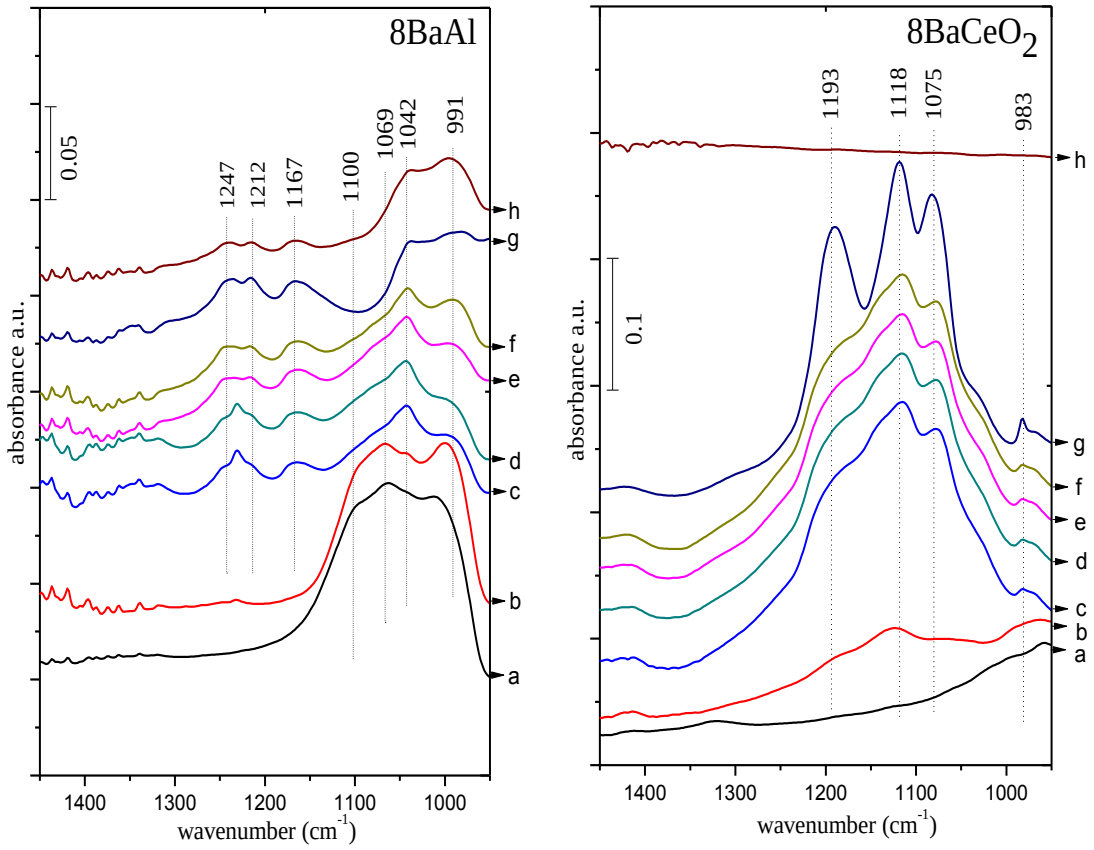

Figure 28: FTIR spectra for SO_2 (g) + O_2 (g) (SO_2:O_2, 0.1:1) co-adsorption on 8BaAl and 8BaCeO$_2$ a) After 10 min exposure to SO_2 (g) + O_2 (g) at 323 K (spectrum was obtained in the presence of the gas mixture), b) after flashing the sample to b) 473 K c) 673 K in SO_2 + O_2 and cooling to 323 K (spectrum was obtained in the presence of the gas mixture), d) after SO_2 (g) + O_2 (g) mixture evacuated ($P_{reactor}$ ~1×10-3 Torr) , after flashing the sample to e) 473K f) 673K g) 873K and h)1073K in vacuum ($P_{reactor}$ < 1×10^{-3} Torr) and cooling to 323 K.

Figure 28 presents the SO_x uptake properties of 8Ba/Al system in comparison to the 8Ba/Ce system. It is visible in figure 26 that during the SO_2 (g) + O_2 (g) exposure at 323 K, 8Ba/Al_2O_3 sample presents broad absorption bands at 1100, 1069, 1042 and 991 cm^{-1}. The bands at 1100 and 1069 cm^{-1} are characteristic for the S-O stretching vibrations of bidentate sulfates located on the surface of BaO [118-120]. These two features were not thermally stable and decomposed at 473 K. Two minor bands located at 1247 cm^{-1} and 1167 cm^{-1} were present on this sample . These vibrational bands can be attributed to bulk barium sulfate species [121].

We also worked on ceria supported 8 wt% BaO material which was prepared by the usual wetness impregnation method as described above. Adsorption of SO_2 (g) + O_2 (g) mixture at 323 K on this surface led to a vibrational band at 1322 cm^{-1} (physisorbed SO_x species) and some other overlapping bands between 1200-950 cm^{-1} in Figure 28. Upon heating in gas mixture at 673 K, four different features at 1193, 1118, 1075 and 983 cm^{-1} were observed. According to several former studies [118-120], none of these features can be assigned to any sulfur content which is related to BaO. However, these bands can be attributed to bulk (1188 and 1120 cm^{-1}) and surface type (983 cm^{-1}) sulfates on CeO_2.

Another important aspect of Figure 28 is that although at T > 673 K, 8Ba/Ce sample seem to uptake a greater quantity of SO_x, 8Ba/Ce sample seems to regenerate more efficiently than the 8Ba/Al sample after annealing at 1073 K in vacuum.

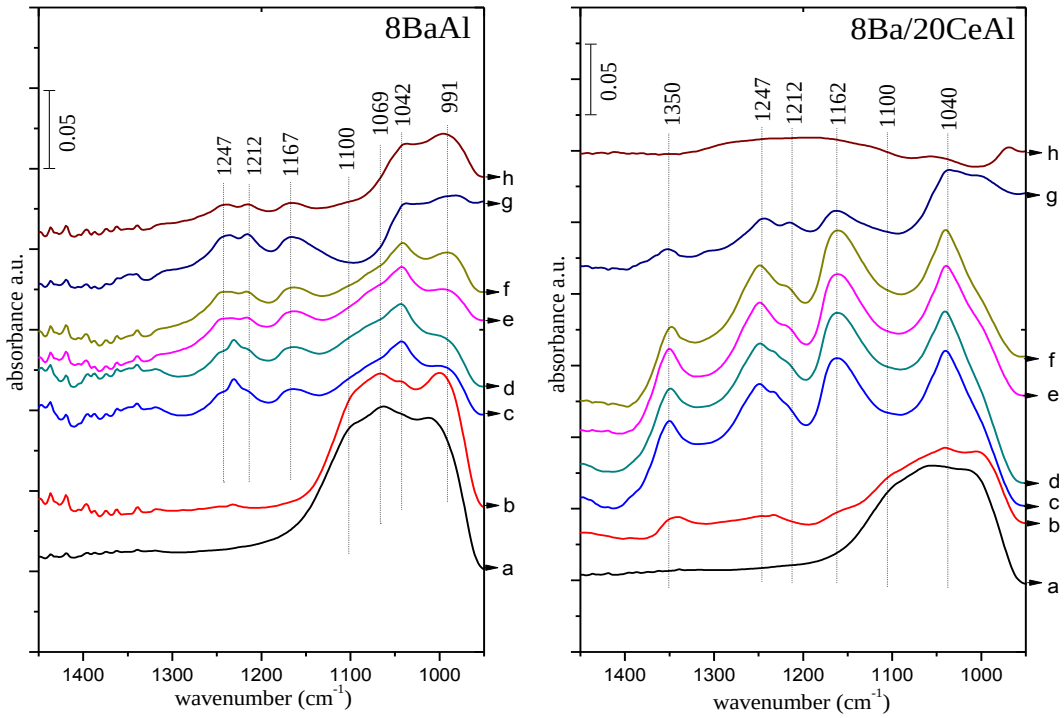

Şekil 29: FTIR spectra for SO_2 (g) + O_2 (g) (SO_2:O_2, 0.1:1) co-adsorption on 8BaAl and 8BaCeO_2 a) After 10 min exposure to SO_2 (g) + O_2 (g) at 323 K (spectrum was obtained in the presence of the gas mixture), b) after flashing the sample to b) 473 K c) 673 K in SO_2 + O_2 and cooling to 323 K (spectrum was obtained in the presence of the gas mixture), d) after SO_2 (g) + O_2 (g) mixture evacuated ($P_{reactor}$ ~1×10-3 Torr) , after flashing the sample to e) 473K f) 673K g) 873K and h)1073K in vacuum ($P_{reactor}$ < 1×10^{-3} Torr) and cooling to 323 K.

Nature of the adsorbed SO_x species were also studied for selected samples such as 8Ba/Al and 8Ba/20Ce/Al (Figure 29). Upon promotion of CeO_2 to alumina support, vibrational band at 1350 cm^{-1} which is due to the surface sulfates started to appear. This feature was thermally stable up to 873 K. Bands due to bulk-like sulfate species on BaO at 1247 and 1167 cm-1 appeared at 673K, for both samples. Another important effect of ceria promotion which we have observed in Figure 29 was associated with the thermal stability of the sulfate species. Spectra obtained after annealing in vacuum at 1073 K, showed that SO_x speices were relatively less stable on the 8Ba/20Ce/Al sample.

3.4 Quantitative SO_x Uptake Determination via XPS

XPS measurements were also performed in order to obtain quantitative information regarding the relative SO_x uptakes of synthesized materials . Prior to XPS analysis, samples were poisoned with 10 Torr of SO_x (SO_2:O_2 = 1: 10) at 673 K for 30 minutes. Figure 30 shows the relative atomic percentile of sulfur atoms with respect to all other atoms on the investigated surfaces (i.e. Al, O, Ba, Ce).

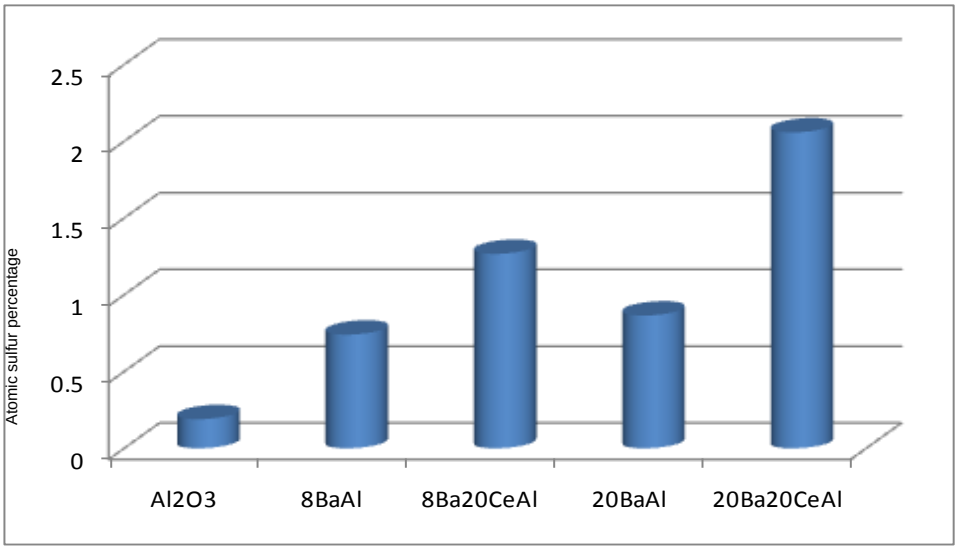

Figure 30: Histogram showing the relative sulfur percentage in the poisoned materials obtained via XPS.

Figure 30 suggests that CeO_2 addition increases the sulfur uptake of the Ba/Al system suggesting that CeO_2 sites function as sacrificial sites when they are exposed to sulfur containing species.

4. CONCLUSION:

Understanding the chemical nature of material surfaces and their interactions chemical environments is a promising way to design and synthesize high performance catalytic materials. In the current work, materials relevant to NSR catalysis were structurally characterized (via XRD, Raman and BET) and their NO_x and SO_x uptake abilities as well the thermal stabilities of the adsorbed species on these surfaces were investigated via FTIR, TPD and XPS techniques.

It was observed that Pt addition and increase in Ba loading typically facilitate the formation of $BaAl_2O_4$ phase for most of the investigated systems. However, ceria addition suppressed the formation of this undesired phase to a certain extent.

Platinum addition to Ce/Al binary oxide and Ba/Ce/Al ternary oxide systems has two major effects; (i) formation of new surface mixed oxide, Pt-O-CeO2, species owing to strong metal support interaction, (ii) decomposition of nitrate species at lower temperatures relative to Pt-free materials.

Ceria promotion of the alumina support material does not significantly alter the nature of the adsorbed nitrate species or the NO_x uptake. However, presence of Pt increases the total NO_x uptake as compared to Pt-free samples. Nitrate decomposition in Pt-containing materials is ~100 K lower than that of the Pt-free materials indicating the catalytic function of the Pt sites in nitrate decomposition.

For Ba/Ce/Al ternary oxide system, increasing baria or ceria loadings results in decreasing specific surface area (SSA) values and attenuated NO_x uptake.

The results from SO_2 (g) + O_2 (g) exposure reveal that ceria promotion to γ-Al_2O_3 enhances the surface sulfate formations. This trend is also observed for the Pt/Ce/Al system Ceria promotion has two major consequences in SO_x interactions of the synthesized materials; (i) materials containing ceria is able to store more SO_x in the temperature range between 673-873K, but less storage in temperature range between 323-473 K, (ii) ceria promotion decreases the thermal stability of the formed sulfates and enhance the regeneration capability of the investigated materials.

5. REFERENCES

[1] S. Erkfeldt, E. Jobsob, M. Larsson, Topics in Catal. 2001, 1, 16.

[2] F. Klingstedt, K. Arve, K. Eranen, D.Y. Murzin, Acc. Chem. Res.2006, 39, 273–282.

[3] Matsumoto, S. Cattech, 2000, 4, 102.

[4] K. Kato, H. Nohira, K. Nakanishi, S. Iguchi, T. Kihara, H. Muraki, Eur. Patent application 0,573,672 A1 (1993).

[5] N. Myioshi, S. Matsumoto, K. Katoh, T. Tanaka, K. Harada, N. Takahashi, K. Yokota, M. Sugiura, K. Kasahara, SAE Technical Papers Series No. 950809, 1995.

[6] L. Lietti, P. Forzatti, I. Nova, E. Tronconi, J. Catal. 204 (2001) 175.

[7] M. Ricken, J. Nölting, I. Reiss, J. Solid State Chem, 54, 89 (1984)

[8] R. Korner, M. Ricken, J. Nölting, I. Riess, J. Solid State Chem, 78, 136, 1989

[9] R. Ranga, B. Mishra, Bulletin of the Catalysis Society of India 2 (2003)122-134

[10] S. Roy, A. Baiker, Chem. Rev. XXXX, xxx, 000–000, Received October 25, 2008

[11] O. Mekasuwandumrong, P. Praserthdam, M. Inoue, V. Pavarajarn, W. Tanakulrungsank, W. J. of Mater. Sci. 2004, 39, 2417.

[12] S.H. Cai, S.N Rashkeev, S.T. Pantelides, K. Sohlberg, Physical Review B 2003, 67, 224104.

[13] Y. Liu, M. Meng, Z. Zou, X.-G. Li, Y. Zha, Catal. Commun. 2008, 10, 173.

[14] Liu, Y.; Meng, M.; Li, X.-G.; Guo, L.-H.; Zha, Y.-Q. Chem. Eng. Res. Des. 2008, 86, 932.

[15] N. Takahashi, A. Suda, I. Hachisuka, M. Sugiura, H. Sobukawa, H. Shinjoh, Appl. Catal. B: EnViron. 2007, 72, 187.

[16] Z.-Q. Zou, M. Meng, N. Tsubaki, J.J. He, G. Wang, X.-G Li, X.-Y. Zhou, J. Hazard. Mater. 2009, 170, 118.

[17] A. Amberntsson, M. Skoglundh, S. Ljungström, E. Fridell, J. Catal. 217 (2003) 253.

[18] J. Breen, M. Marella, C. Pistarino, J.RH. Ross, Catal. Lett. 80 (2002) 123.
[19] K. Yamazaki, T. Suzuki, N. Takahashi, K. Yokota, M. Sugiura, Appl. Catal. B 30 (2001) 459.
[20]F. Rohr, S.D. Peter, E. Lox, M. Kogel, A. Sassi, L. Juste, C. Rigaudeau, G. Belot, P. Gelin,

[21] M. Casapu, J. Grunwaldt, M. Maciejewski, M. Wittrock, U. Go¨ bel, A. Baiker, Appl.Catal. B 63 (2006) 232.

[22] M.A. Peralta, V.G. Milt, L.M. Cornaglia, C.A. Querini, J. Catal. 242 (2006) 118.
[23] E. Corbos, X. Courtois, N. Bion, P. Marecot, D. Duprez, Appl. Catal. B 80 (2008) 62.
[24] J. Kwak, D. Kim, J. Szanyi, C.H.F. Peden, Appl. Catal. B 84 (2008) 545.
[25] M. Ozawa, J. Alloys Compd. 275–277 (1998) 886.
[26] J. Kaspar, P. Fornasiero, M. Graziani, Catal. Today 50 (1999) 285.
[27] S.I. Matsumoto, Catal. Today 90 (2004) 183.
[28] A. Trovarelli (Ed.), Catalysis by Ceria and Related Materials, Imperial College Press, London, 2002.
[29] J.Z. Shyu, K. Otto, J. Catal. 115 (1989) 16.
[30] Y. Nagai, T. Hirabayashi, K. Dohmae, N. Takagi, T. Minami, H. Shinjoh, S.I. Matsumoto, J. Catal. 242 (2006) 103.
[31] S. Hilaire, X. Wang, T. Luo, R.J. Gorte, J. Wagner, Appl. Catal. A 215 (2001) 271.
[32] P. Panagiotopoulou, D.I. Kondarides, Catal. Today 112 (2006) 49.
[33] A. Haryanto, S. Fernando, N. Murali, S. Adhikari, Energy Fuels 19 (2005) 2098.
[34] F. Frola, F. Prinetto, G. Ghiotti, L. Castoldi, I. Nova, L. Lietti, P. Forzatti, Catal. Today 126 (2007) 81.
[35] I. Malpartida, M.O. Guerrero-Pe´ rez, M.C. Herrera, M.A. Larrubia, L.J. Alemany,
Catal. Today 126 (2007) 162.
[36] U. Elizundia, R. Lo´ pez-Fonseca, I. Landa, M.A. Gutie´ rrez-Ortiz, J.R. Gonza´ lez- Velasco, Top. Catal. 42–43 (2007) 37.
[37] Y. Su, K.S. Kabin, M.P. Harold, M.D. Amiridis, Appl. Catal. B 71 (2007) 207.

[38] H. Abdulhamid, J. Dawody, E. Fridell, M. Skoglundh, J. Catal. 244 (2006) 169.
[39] I. Nova, L. Castoldi, L. Lietti, E. Tronconi, P. Forzatti, F. Prinetto, G. Ghiotti, J. Catal. 222 (2004) 377.
[40] C. Paze´, G. Gubitosa, S. Orso Giacone, G. Spoto, F.X. Llabre´ s i Xamena, A. Zecchina, Top. Catal. 30/31 (2004) 169.
[41] Y. Su, M.D. Amiridis, Catal. Today 96 (2004) 31.
[42] F. Prinetto, G. Ghiotti, I. Nova, L. Castoldi, L. Lietti, E. Tronconi, P. Forzatti, Phys. Chem. Chem. Phys. 5 (2003) 4428.
[43] Ch. Sedlmair, K. Seshan, A. Jentys, J.A. Lercher, J. Catal. 214 (2003) 208.
[44] T. Lesage, C. Verrier, P. Bazine, J. Saussey, M. Daturi, Phys. Chem. Chem. Phys. 5 (2003) 4435.
[45] F. Prinetto, G. Ghiotti, I. Nova, L. Lietti, E. Tronconi, P. Forzatti, J. Phys. Chem. B 105 (2001) 12732.
[46] S. Philipp, A. Drochner, J. Kunert, H. Vogel, J. Theis, E.S. Lox, Top. Catal. 30/31 (2004) 235.
[47] M.O. Symalla, A. Drochner, H. Vogel, S. Philipp, U. Go¨bel, W. Mu¨ller, Top. Catal. 42/43 (2007) 199.
[48] F. Epron, F. Gauthard, C. Pineda and J. Barbier, J. Catal. 198 (2) (2001), pp. 309–318

[49] B. Harrison, A.F. Diwell, C. Hallett, Platinum Met. ReV. (1988), 32, 73.
[50] G. Leclercq, C. Dathy, C. Mabilon, L. Leclercq, Stud. Surf. Sci. Catal. (1991), 71, 181.

[51] C. Paze, G. Gubitosa, S.O. Giacone, G. Spoto, F.X.L. Xamena, A. Zecchina, Top. Catal. 30–31 (2004) 169.
[52] S. Roy, A. Baiker, Chem. Rev. 2009, 109, 4054
[53] P. Forzatti, L. Castoldi, I. Nova, L. Lietti, E. Tronconi, Catal. Today 2006, 117, 316

[54] J.A. Anderson, B. Bachiller-Baeza, M. Fernandez-Garcia, Phys. Chem. Chem. Phys. 2003, 5, 4418.

[55] V. Medhekar, V. Balakotaiah, M.P. Harold, Catal. Today 2007, 121, 226.

[56] B. Jang, T. Yeon, H. Han, Y. Park, J. Yie, Catal. Lett. 77 (2001) 21.

[57] D. Kim, Y. Chin, J. Kwak, J. Szanyi, C.H.F. Peden, Catal. Lett. 105 (2005) 259.
[58] G. Graham, H. Jen, W. Chun, H. Sun, X. Pan, R. McCabe, Catal. Lett. 93 (2004) 129.
[59] S. Elbouazzaoui, X. Courtois, P. Marecot, D. Duprez, Top. Catal. 30/31 (2004) 493.

[60] D. Uy, K.A. Wiegand, A.E. O'Neill, M.A. Dearth, W.H. Weber, J. Phys. Chem. B 106 (2002) 387.

[61] S. Elbouazzaoui, E.C. Corbos, X. Courtois, P. Marecot, D. Duprez, Appl. Catal. B 61 (2005) 236.

[62] P. Engström, A. Amberntsson, M. Skoglundh, E. Fridell, G. Smedler, Appl. Catal. B: Environ. 22 (1999) L241.
[63] E. Fridell, H. Persson, L. Olsson, B. Westerberg, A. Amberntsson, M. Skoglundh, Top. Catal. 16/17 (2001) 133.
[64] A. Amberntsson, M. Skoglundh, M. Jonsson, E. Fridell, Catal. Today 73 (2002) 279.
[65] A. Amberntsson, B. Westerberg, P. Engström, E. Fridell, M. Skoglundh, Stud. Surf. Sci. Catal. 126 (1999) 317.
[66] A. Amberntsson, M. Skoglundh, S. Ljungström, E. Fridell, J. Catal. 217 (2003) 253
[67] J.P. Breen,M. Marella, C. Pistarino, J.R.H. Ross, Catal. Lett. 80 (2002) 123
[68] C. Courson, A. Khalfi, H. Mahzoul, S. Hodjati, N. Moral, A. Kiennemann, P. Gilot, Catal. Commun. 3 (2002) 471.
[69] H. Mahzoul, L. Limousy, J.F. Brilhac, P. Gilot, J. Appl. Pyrol. 56 (2000) 179.
[70] M. Waqif, P. Bazin, O. Saur, J.C. Lavalley, G. Blanchard, O. Touret, Appl. Catal. B (1997) 193-205
[71] G. Cavell, A. Datta, W. Tower, M. Gearge, J. Phys. Chem. 1985. 89, 443
[72] C. Chang, Journal of Catalyst, 1978, 53, 374-385
[73] M. Waqif, A. Pieplu, O. Saur, J.C. Lavalley, G. Blanchard, Solid State Ionics 1997 163
[74] M. Waqif, P. Bazin, O. Saur, J.C. Lavalley, G. Blanchard, O. Touret, Appl. Catal. B (1997) 193-205

[75] O. Saur, M. Bensitel, A.B. Mohammed Saad, J.C. Lavalley, C.P. Tripp and B.A. Morrow. J. Catal. 99 (1986), p. 104.
[76] Y. Ji, T.J. Topps, M. Crocker, Catal. Lett. 127 (2009) 55.
[77] P. Bazin, O. Saur, J.C. Lavalley, G. Blanchard, V. Visciglio, O. Touret
[78]H. Yao, H. Stepien, H. Gandhi, J. Catal. 67 (1981) 231.
[79]A. Melchor, E. Garbowski, M. Mathieu, M. Primet, React. Kinet. Catal. Lett. 29 (1985) 371.
[80] Li-Dun, Deng You Quan, Appl. Catal. 66 (1990) 219.
[81]T. Luo, J.M. Vohs, R.J. Gorte, Journal of catalysis 210, 397-404 (2002)
[82] T. Yu, H. Shaw, Appl Catal. B18 (1998) 105-114
[83] S. Colussi, F. Arosio, T. Montanari, G. Busca, G. Groppi, A. Trovaralli, Catalysis Today155 (2010) 59-65
[84] M. Boaro, C. de Leitenburg, G. Dolcetti, A. Trovarelli, M. Graziani, Top. Catal. 16/17 (2001) 299–306.
[85] D.L. Mowery, R.L. McCormick, Appl. Catal. B 34 (2001) 287–297.
[86] L. Kylhammar, P. Carlsson, H. Ingelsten, H. Grönbeck, M. Skoglundh, Applied Catalysis B 84 (2008) 268-276
[87] H. Abdulhamid, E. Fridell, J. Dawody, M. Skoglundh, Journal of Catalysis 241 (2006) 200-210
[88] Y. Su, D. Amiridis, Catalysis Today 96 (2004) 31-41
[89] E. Kayhan, a thesis, structure and NOx uptake properties of Fe-promoted storage materials, June 2009
[90] D. Uy, A.E. O'Neill, J. Li, W.L.H Watkins, Catal. Lett. 2004, 95 (3-4), 191.
[91] F. Frola, M. Manzoli, F. Prinetto, G. Ghiotti, L. Castoldi, L. Lietti, J.Phys.Chem. C 112 (2008)33
[92] J. Z. Shyu, W. H. Weber and H. S. Ghandi, J. Phys. Chem., 1988, 92,4964.
[93] M.S. Brogan, J. Dines, A. Cairns, J. Chem. Soc. Faraday Trans., 1994, 90, 1461
[94]H. C. Tao and Y. F. Yu Yao, J. Catal., 1984,86,254.
[95]K. Nakamoto, Infrared and Raman Spectra of Inorganic and Coordination Compounds, Wiley, New York, 4th edn., 1988.
[96] E. Ozensoy, D. Herling, J. Szanyi, Cat. Today. 136 2008 46-54

[97] Ch. Sedlmair, K. Seshan, A. Jentys, J.A. Lercher, J. Catal. 214 (2003) 308.

[98] B. Westerberg, E. Fridell, J. Mol. Catal. A: Chem. 165 (2001) 249.

[99] W.S. Kijlstra, D.S. Brand, E.K. Poels, A. Bliek, J. Catal. 171 (1997) 208.

[100] J.P. Breen, M. Marella, C. Pistarino, J.R.H. Ross, Catal. Lett. 80 (2002) 123.

[101] K. Hadjiivanov, V. Bushev, M. Kantcheva, D. Klissurski, Langmuir, 1994,

[102] J. Szanyi, J.H. Kwak, R.J. Chimentao, C.H.F. Peden, J. Phys. Chem. C, 2007, 111,2661.

[103] E. Ozensoy, D. Herling, J. Szanyi, Catal. Today, 2008, 136, 46.10, 464.

[104] E. Kayhan, S.M. Andonova, G.S. Şentürk, C.C Chusuei, E. Ozensoy, J. Phys. Chem. C, 2010, 114, 357.

[105] J.H. Kwak, D. Mei, Ch.-W. Yi, D.H. Kim, C. H. F. Peden, F. Allard, J. Catal. 2009, 261, 17.

[106] J. Szanyi, J. H. Kwak, D. H. Kim, S. D. Burton, C. H. F. Peden, J. Phys. Chem. B 2005, 109, 27.

[107] T. Venkov, K. Hadjiivanov, D. Klissurski, Phys. Chem. Chem. Phys. 2002, 4, 2443.

[108] J. Szanyi, J. H. Kwak, R. J. Chimentao, Ch. F. Peden, J. Phys. Chem. C 2007, 111, 2661.

[109] M. Digne, P. Sautet, P. Raybaud, P. Euzen, H. Toulhoat, J. Catal. 2004, 226, 54.

[110] J. H. Kwak, J. Z. Hu, D. H. Kim, J. Szanyi, C. H. F. Peden, J.Catal. 2007, 251, 189.

[111] B. Westerberg, E. Fridell, J. Mol. Catal. A: Chem. 165 (2001) 201.

[112] F. Prinetto, G. Ghiotti, I. Nova, L. Lietti, E. Tronconi, P. Forzatti, J. Phys. Chem. B 105 (2001) 105.

[113] H.Y. Huang, R.Q. Long, R.T. Yang, Energy Fuels 15 (2001) 205.

[114] C. Sedlmair, K. Seshan, A. Jentys, J.A. Lercher, J. Catal. 214 (2003) 308.

[115]M. B. Mitchell, N. Sheinker, J. Phys. Chem., 1996, 100, 7550.

[116] C. C Chang, J. Catal,. 1978, 53, 374.

[117] Davydov, A.A., Molecular spectroscopy of oxide catalyst surfaces, Wiley, Chichester, England, 2003

[118] R. A.Schoonheydt, J. H. Lunsford, J. Catal., 1972, 26, 261.

[119] M.A. Babaeva, A.A. Tsyganenko, V.N. Filimonov, Kinet. Katal. 1985, 787.
[120] C. Sedlmair, K. Seshan, A. Jentys, J. A. Lercher, Catal. Today, 2002, 75,413.
[121] M. Waqif, J. C. Lavelly, S. Perathoner, G. Centi, J. Phys. Chem., 1991, 95, 4051.